JGR Atmospheres

RESEARCH ARTICLE
10.1029/2024JD041294

Exploring Sources of Gravity Waves in the Southern Winter Stratosphere Using 3-D Satellite Observations and Backward Ray-Tracing

Phoebe E. Noble[1,2], Sebastian Rhode[3,4], Neil P. Hindley[1], Peter Berthelemy[1,2], Tracy Moffat-Griffin[2], Peter Preusse[3,4], Lars Hoffmann[4,5], and Corwin J. Wright[1]

[1]Department of Electronic Engineering, Centre for Climate Adaptation & Environment Research, University of Bath, Bath, UK, [2]Atmosphere, Ice and Climate Team, British Antarctic Survey, Cambridge, UK, [3]Institute of Energy and Climate Research, Stratosphere (IEK-7), Forschungszentrum Jülich, Jülich, Germany, [4]Center for Advanced Simulation and Analytics (CASA), Forschungszentrum Jülich, Jülich, Germany, [5]Jülich Supercomputing Center (JSC), Forschungszentrum Jülich, Jülich, Germany

Key Points:

- We use gravity wave properties derived from stratospheric satellite observations as input to a backward ray-tracing model
- Ray-tracing reveals that gravity waves observed at all longitudes around the Southern Ocean converge to 60°S as they propagate upward
- We quantify the momentum flux (MF) from different regions, finding that, in winter 2012, over half of the MF is traced back to the ocean

Supporting Information:

Supporting Information may be found in the online version of this article.

Correspondence to:

P. E. Noble,
pn399@bath.ac.uk

Citation:

Noble, P. E., Rhode, S., Hindley, N. P., Berthelemy, P., Moffat-Griffin, T., Preusse, P., et al. (2024). Exploring sources of gravity waves in the southern winter stratosphere using 3-D satellite observations and backward ray-tracing. *Journal of Geophysical Research: Atmospheres*, *129*, e2024JD041294. https://doi.org/10.1029/2024JD041294

Received 3 APR 2024
Accepted 16 NOV 2024

Abstract During austral winter, the southern high latitudes has some of the most intense stratospheric gravity wave (GW) activity globally. However, producing accurate representations of GW dynamics in this region in numerical models has proved exceptionally challenging. One reason for this is that questions remain regarding the relative contributions of orographic and non-orographic sources of GWs here. We use three-dimensional (3-D) satellite GW observations from the Atmospheric Infrared Sounder in austral winter 2012 in combination with the Gravity-wave Regional Or Global Ray Tracer to backward trace GW rays to their sources. We trace over 14.2 million rays, through ERA5 reanalysis background atmosphere, to their lower atmospheric sources. We find that GWs observed thousands of km downstream can be traced back to key orographic regions, and that on average, all waves (orographic and non-orographic) converge meridionally over the Southern Ocean. We estimate that across this winter, orographic sources contribute around ∼5%–35% to the total momentum flux (MF) observed near 60°S. The remaining proportion consists of waves from non-orographic sources, which although typically carry lower MF, the large spatial extent of non-orographic sources leads to a higher overall contribution. We also quantify the proportion of MF traced back to different regions across the whole southern high latitudes area in order to measure the relative importance of these different regions. These results provide the important insights needed to advance our knowledge of the atmospheric momentum budget in the southern high latitudes.

Plain Language Summary Just like the ocean, our atmosphere contains waves which transport energy and momentum. These atmospheric waves, known as gravity waves (GWs), strongly influence large-scale wind patterns but are hard to represent in climate models. The Southern Hemispheric stratosphere has some of the strongest GW activity on our planet and accurately representing this region in models has proved exceptionally challenging. Further, inaccurate representations of gravity waves can lead to major model biases. Here, we use satellite observations of stratospheric GWs and, using new methods, identify GWs and measure GW amplitudes, wavelengths, and directions. We then use these observations in combination with a ray-tracing model to track observed GWs back to their sources near the ground. This approach means that, for the first time, we are able to produce systematic estimates of the relative contribution of different wave sources to the observed stratospheric activity in the southern high latitudes.

1. Introduction

Atmospheric gravity waves (GWs) play a major role in the vertical coupling, transporting momentum and driving the circulation at high altitudes, in particular the overarching mesospheric circulation branch (Fritts & Alexander, 2003). Misrepresentation of GWs in General Circulation Models can lead to major circulation biases.

During austral winter, the Southern Hemisphere high-latitude stratosphere is one of the world's strongest regions of GW activity (Alexander et al., 2010; Hertzog et al., 2012; Hindley et al., 2020, 2015; Hoffmann et al., 2013; Wright et al., 2016; and many others). Here, maps of GW activity are dominated by orographic waves from the Southern Andes and Antarctic Peninsula. Small islands such as South Georgia (Hindley et al., 2020) and Kerguelen (Alexander & Grimsdell, 2013) are sparsely scattered across Southern Ocean and also act as strong local

sources (Hoffmann et al., 2016), generating wakes of GW activity which stretch hundreds of km downstream (Alexander et al., 2009). Additionally, intense GW activity is found all around the 60°S belt over open ocean and is believed to be generated by non-orographic sources such as storms, frontogenesis, and jet adjustment processes around the edge of the polar vortex (Hendricks et al., 2014; Hindley et al., 2015; Holt et al., 2017, 2023; Plougonven et al., 2017; Strube et al., 2021; Wu & Eckermann, 2008). Uniform westerly wind conditions that increase with altitude during winter allow GWs generated in the lower atmosphere to propagate upward through the stratosphere without encountering critical levels, where their momentum deposition can have a major impact on the global general circulation by decelerating the background winds (Polichtchouk et al., 2018).

Due to computational limitations, most climate models use parameterizations of subgrid-scale GW dynamics; however, these can have significant negative consequences. For example, it is widely hypothesized that missing GW drag in models is a primary cause underlying the "cold pole" bias (Alexander & Grimsdell, 2013; Holt et al., 2023; McLandress et al., 2011), whereby the Southern Hemisphere polar stratosphere is too cold in winter and the polar stratospheric vortex breaks down too late in spring relative to observations. Supporting this hypothesis, models persistently show a significant local reduction in stratospheric GW momentum flux (MF) at 60°S in disagreement with observations (Geller et al., 2013; Holt et al., 2023).

Although the community agrees that the cold pole bias is primarily due to missing GW drag, the source of the GWs that produce this drag remains a topic of major debate (de la Cámara et al., 2016; Gupta et al., 2021). Previous studies suggest that at least a proportion of the missing flux can be explained by the lateral focusing of GWs from sources poleward and equatorward of 60°S. This lateral propagation of GWs is not included in model parametrizations (Plougonven et al., 2020) but has been demonstrated in ray-tracing model experiments by Sato et al. (2011) and Rhode et al. (2023) and has shown to be consistent with observed directional GW properties observed by Wright et al. (2017), Hindley et al. (2015), and Moffat-Griffin et al. (2020).

Other work, meanwhile, highlights underrepresented orographic MF from small islands in the Southern Ocean as a possible source of missing drag. In NASA's Goddard Earth Observing System Chemistry Climate Model (GEOS CCM), Garfinkel and Oman (2018) increased the orographic wave drag over three small islands in the Southern Ocean to near observed levels and found a reduction in the cold pole bias. Observationally, meanwhile, Hoffmann et al. (2016) explored GW activity from 18 hotspots (regions of enhanced GW activity), including small islands in the Southern Ocean using AIRS satellite data, and concluded that mountain waves at these hotspots contribute significantly to overall observed MF. MF from these small islands is often vastly underestimated in models as the island size is much smaller than the model grid cell (Alexander et al., 2009). Finally, research has highlighted the importance of non-orographic GWs, which can be generated across the large spatial area of the Southern Ocean and may hence integrate to make a large overall contribution to total MF at these latitudes (Dörnbrack et al., 2022; Hertzog et al., 2008; Jewtoukoff et al., 2015; Plougonven et al., 2013, 2020).

Garcia et al. (2017) explored the modification of the Whole Atmosphere Community Climate Model's GW parametrization and noted that increasing orographic GW forcing reduced the cold pole bias; however, other approaches to enhance GW activity can also reduce the bias. Separately, Eichinger et al. (2023) found a reduction in model biases by implementing a parametrization that included lateral group propagation. These modeling studies demonstrate that there are multiple possible ways to reduce this bias and this highlights the need for observational work to provide knowledge on the missing sources of GW drag near 60°S. Untangling the sources of GWs in this region, their relative importance and their propagation behavior could provide a key way to address this knowledge gap. This would in turn help advance subseasonal-to-seasonal weather predictions and climate modeling, reduce the cold pole bias, and simultaneously address many other problems arising in this region from the poor simulation of GW effects.

Spatial ray-tracing methods provide an ideal tool for tackling this problem and have consequently been employed previously in various GW studies. Spatial ray-tracing is a numerical method for deriving the spatial group propagation trajectory of a slowly varying linear GW packet through a prescribed background atmosphere, while conforming to the WKB condition. Previous forward-tracing work has used model-derived (for instance Preusse et al., 2014; Sato et al., 2011; Vosper, 2015), observationally determined (Krasauskas et al., 2023; Pramitha et al., 2020; Preusse et al., 2009) or idealized (Alexander, 1998; Amemiya & Sato, 2016; Q. Jiang et al., 2019;

Preusse et al., 2002) GW properties to initialize GWs and explore their propagation through model/reanalysis background fields. More recently, forward ray-tracing has been explored as a way of including lateral propagation into model GW parametrizations (Amemiya & Sato, 2016; Eichinger et al., 2023; Voelker et al., 2024).

Backward ray-tracing, where GW properties are defined later in the GW's lifecycle allows for the determination of GW sources. Observations are often use to constrain these back traces, for example, radiosonde observations (Pulido et al., 2013), airglow observations (Wrasse et al., 2006), and Krisch et al. (2017) used observations of a GW event over Iceland from the aircraft-based Gimbaled Limb Observer for Radiance Imaging of the Atmosphere (GLORIA) and traced the waves forward and backward from 11.5 km altitude. More recently, Perrett et al. (2020) used 1 month of AIRS observations to constrain backward tracing in the Southern Hemisphere, providing a proof of concept we expand upon in this study.

Backward ray-tracing GWs characterized in AIRS nadir imagery can be a particularly powerful method for untangling GW source mechanisms in the Southern Hemisphere. The observed 3-D wave vector is fully characterized by using a 3-D AIRS retrieval and the recently developed 3-D spectral analysis technique which allows for full 3-D inputs for ray-tracing. Additionally, our use of satellite data as the input for back-tracing allows for spatial coverage that ground-based or radiosonde observations cannot achieve. This specifically allows us to explore (a) focusing of GWs to 60°S, (b) downstream propagation of orographic GWs, (c) spatial distribution of MF from orographic and non-orographic sources, and (d) MF originating from different source regions across the southern high latitudes.

We present the data in Section 2 and Section 3 describes the methods used to obtain GW properties and perform the ray-tracing. Results are presented and discussed in Section 4 and we conclude our work in Section 5.

2. Data

2.1. 3-D Gravity Wave Observations From AIRS

We use stratospheric GW observations made in southern polar winter from May to September 2012 by the Atmospheric Infrared Sounder (AIRS) onboard the National Aeronautics and Space Administration's (NASA) Aqua satellite (Aumann et al., 2003; Chahine et al., 2006). Aqua was launched in 2002 and is still operating. Aqua follows a near-polar orbit with a period of ≈100 minutes. We chose 2012 for this work as it was a non-extreme year for the Quasi-biennial Oscillation (QBO) and the El Niño Southern Oscillation (ENSO). This was measured for the QBO using the zonal-mean zonal winds at 50 hPa from NCEP/NCAR reanalysis, and for ENSO using Nino 3.4 index (see Figure 1 of Suneeth and Das (2020)). The QBO and ENSO have been found to have far reaching teleconnections and this may affect high latitude stratospheric GW activity, in particular Llamedo et al. (2019) found a systematic 3.5–4 years oscillation in GW activity observed by a lidar at Rio Gallegos, Argentina (51S). The QBO is also found to correlate with high latitude stratospheric winds Anstey and Shepherd (2014). As such, by choosing to study 2012, we expect this year to be broadly representative of other non-extreme years.

AIRS is a nadir viewing hyperspectral imager and measures atmospheric radiances in a cross-track sampling geometry. The data have a swath width of 1 780 km with a resolution of 13.5 km (across-track) × 18 km (along-track) at the nadir, which reduces toward the edges of the swath (Hoffmann et al., 2014). We use the 3-D temperature retrieval of Hoffmann and Alexander (2009); this retrieval covers a height range of 20–60 km and only uses channels where the radiance originates entirely in the stratosphere. This means that unlike the Level 2 operational temperature retrieval (Goldberg et al., 2003), the retrieval of Hoffmann and Alexander (2009) does not reduce the resolution to allow for cloud removal and thus instead can use the instrument's full sampling resolution.

No single measurement technique can yet observe the full spectrum of GWs, and observations will be sensitive to specific scales depending on observational and methodological characteristics; this issue is known as the observational filter. The observational filter of different observational techniques for measuring GWs is described in more detail by Alexander et al. (2010) and Wright et al. (2016). Hindley et al. (2019) investigated the observational filter of AIRS by characterizing the sensitivity of the Hoffmann and Alexander (2009) retrieval. This retrieval was found to be almost 100% sensitive to GWs with vertical wavelengths between 35 and 45 km and horizontal wavelengths less than 500 km. However, this sensitivity fell with decreasing vertical wavelength and increasing horizontal wavelength. For example, wavelengths <17 km in the vertical and >1,000 km in the

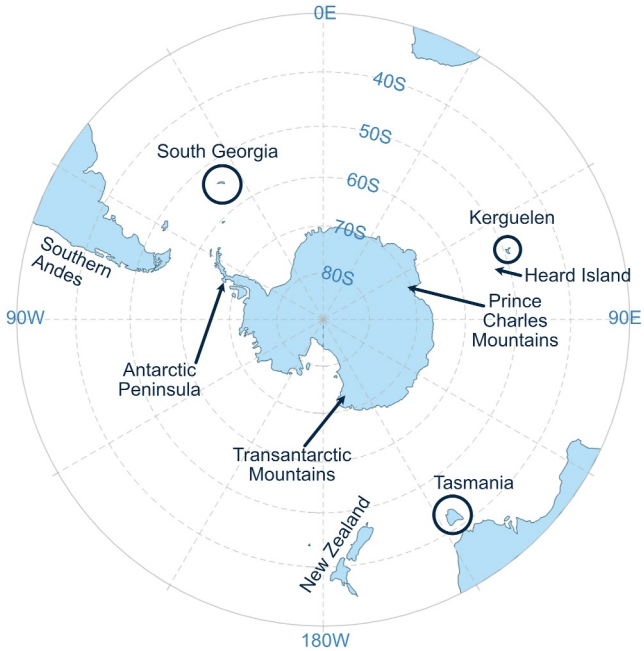

Figure 1. The Southern Hemisphere study region. Key geographical regions are identified with labels.

horizontal are less than 50% sensitive, see Figure 2c of Hindley et al. (2019). GWs with shorter horizontal and longer vertical wavelengths carry the majority of GW MF, making AIRS observations suitable for characterizing MF (Wright et al., 2021). The noise of this retrieval was quantified by Hindley et al. (2019) and is ∼1.5 K for the Southern-Hemisphere winter. The study region is presented in Figure 1 with labels for the key regions we discuss in this paper.

2.2. ERA5 Reanalysis

We use data from the widely used reanalysis product produced by the European Center for Medium-Range Weather Forecasting (ECMWF) known as ERA5 reanalysis (Hersbach et al., 2020). We use the fifth version on model levels to provide large-scale winds for context and background fields for ray-tracing. We use zonal and meridional wind, surface pressure, geopotential, and temperature at three-hourly time resolution interpolated to an equidistant height grid from the geopotential. The 3D pressure field is interpolated from the model hybrid levels and the surface pressure. We remove small-scale perturbations using the separation of scales method that is, by applying a spectral cutoff at zonal wavenumber 18 described by Strube et al. (2021) and smooth in the meridional and vertical directions. We then interpolate this background onto a 1° × 1° latitude-longitude grid, with a 0.5 km vertical resolution between 2 and 39 km altitude. Due to the high topography of the Southern Andes and parts of Antarctica, we do not trace rays below 2 km altitude and consider this to represent the ground level.

3. Method

3.1. Deriving Gravity Wave Properties From AIRS Data

We remove the large-scale temperature variations from AIRS observations by subtracting a fourth-order polynomial in the cross-track direction at each height (e.g., Alexander & Barnet, 2007; Hindley et al., 2019; Hoffmann et al., 2016; Wright et al., 2017; Wu, 2004). We next re-grid the data onto a regular spatial grid and perform spectral analysis to derive GW properties.

We use a three dimensional spectral analysis method known as the 2D+1 S-transform (ST) method described by Wright et al. (2021). This method uses a 2D-ST in the horizontal in combination with vertical phase shift estimation to compute horizontal and vertical wavelengths and corresponding amplitudes. Unlike a Fourier transform, the ST lets us spatially locate amplitude peaks and is commonly used in GW analysis (e.g., Alexander et al., 2008; Fritts et al., 1998; McDonald, 2012; Wright & Gille, 2013). The 2D+1 method builds upon the 1D method originally applied to AIRS data by Alexander and Barnet (2007), the subsequent 2D method developed by Hindley et al. (2016), and is a refinement of the 3-D method described in Hindley et al. (2019) and first applied in Wright et al. (2017). As discussed in Hindley et al. (2020), since AIRS measurements are instantaneous in time, we have ambiguity in the direction of propagation of the waves. As in Hindley et al. (2020) we enforce that all GWs propagate upward. Next, we identify GWs in the data by locating regions of consistent horizontal wavelength. This relies on the premise that GWs have approximately consistent horizontal wavelengths across their extent, whereas background noise leads to random wavelength measurements for each pixel with no relation to their neighbors. The method produces a binary mask identifying whether or not a wave is present for each pixel of AIRS data.

We use the 39 km altitude data level, which lies at the center of AIRS's useful retrieval height range and thus provides the greatest range of vertical wavelengths that can be measured by avoiding "cone of influence" effects. This level also exhibits low noise relative to other heights (Hindley et al., 2019).

Finally, following Ern et al. (2004), we calculate absolute vertical flux of horizontal pseudo-momentum (hereafter simply "absolute MF") at the observation height as given below:

$$|\mathrm{MF}| = \sqrt{\mathrm{MF_x}^2 + \mathrm{MF_y},^2} \tag{1}$$

$$(\mathrm{MF_x}, \mathrm{MF_y}) = -\frac{\rho}{2m}\left[\frac{g}{N}\right]^2\left[\frac{T'}{\bar{T}}\right]^2 (k, l), \tag{2}$$

where $\mathrm{MF_x}$ and $\mathrm{MF_y}$ are the zonal and meridional MF respectively. k and l represent the horizontal wavenumbers in the zonal and meridional directions, and m in the vertical; g is acceleration due to gravity, N is the Brunt Väisälä frequency, which we assume to be 0.02 s^{-1} in the stratospheric MF calculation, and T' and $\bar{T}$ are the wave amplitude and background temperature, respectively. ρ is the atmospheric density. We note that Equation 2 is an approximation to the pseudo-momentum flux in the mid-frequency part of the spectrum as shown in Ern et al. (2004).

As previously discussed in the data section, AIRS is particularly sensitive to short horizontal and long vertical wavelength waves which means it cannot observe certain parts of the spectrum. It is important to highlight that this is a continuous sensitivity, AIRS is most sensitive to horizontal wavelengths less than ~500 km and vertical wavelengths ~ 30–50 km long (Hindley et al., 2019), but this sensitivity decreases with decreasing vertical wavelength and increasing horizontal wavelength. Importantly this reduction in sensitivity carries through to the estimations of momentum fluxes via Equation 2 above. This means that when considering MF derived from AIRS observations in general we must remember that (a) this is not a full estimation of momentum fluxes in the stratosphere due to AIRS not observing all the waves and (b) even for waves that are observed, their MF can be attenuated for waves with wavelengths that AIRS is not 100% sensitive to. For the later, this is particularly relevant for waves that get refracted the longer vertical wavelengths in the strong winds of the polar vortex, and so their MF will be artificially increased relative to waves that do not get refracted to longer vertical wavelengths.

3.2. Backward Ray-Tracing

We use the Gravity wave Regional Or Global Ray Tracer (GROGRAT), originally introduced in Marks and Eckermann (1995), which describes the position and wavenumber along the raypath as:

$$\frac{d\mathbf{x}}{dt} = \frac{\partial\omega}{\partial\mathbf{k}}, \frac{d\mathbf{k}}{dt} = -\frac{\partial\omega}{\partial\mathbf{x}}, \tag{3}$$

where $\mathbf{x}$ and $\mathbf{k}$ are vectors denoting the wave's spherical position and wavenumbers, respectively, and ω is the wave's ground-based frequency expressed by the dispersion relation.

GROGRAT was initially designed to trace waves forward in time, that is, to determine wave propagation from a specified source and properties. A later update to GROGRAT (Eckermann & Marks, 1997) allowed for backward ray-tracing of waves, and we use this approach. We use a modified version of GROGRAT, which incorporates the great-circle correction described by Hasha et al. (2008).

Each pixel of AIRS data that is associated with a wave is used to initialize a separate ray. We calculate the intrinsic frequency $(\hat{\omega})$ as given below:

$$\hat{\omega}^2 = \frac{\mathrm{N}^2\left(k^2 + l^2\right) + f^2\left(m^2 + \frac{1}{4H^2}\right)}{k^2 + l^2 + m^2 + \frac{1}{4H^2}} \tag{4}$$

and use the ERA5 background winds to convert this to ground-based frequency $\left(\omega^2\right)$,

$$\omega = \hat{\omega} + ku + lv. \tag{5}$$

$f = 2\Omega \sin\phi$ is the Coriolis parameter at latitude ϕ and Ω is the rotation rate of the Earth. $H = 7$ km is the density scale height and u and v are the ERA5 background zonal and meridional winds.

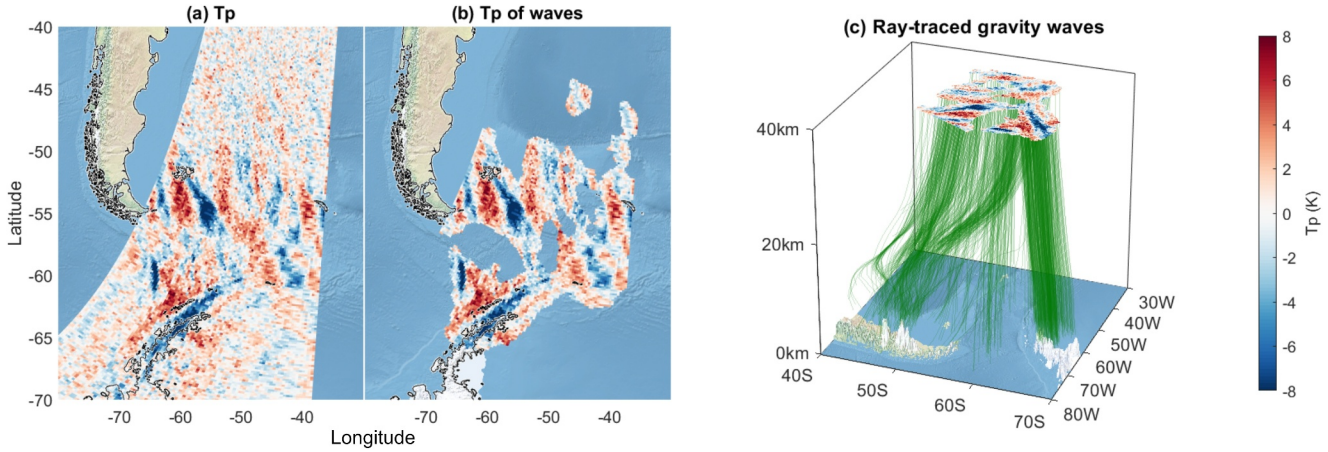

Figure 2. An example of a ray-traced overpass from AIRS from 4 June 2010 at approximately 04:00 UTC. Panel (a) shows the temperature perturbations at 39 km from AIRS. Panel (b) shows the temperature perturbations of pixels that are identified as GWs. Panel (c) shows the ray-tracing. The original masked GWs are shown at the top with rays colored in green descending back toward the Southern Andes and Antarctic Peninsula mountain ranges. Each pixel of AIRS data is used to initialize a ray at 39 km.

Finally, we calculate the horizontal wind amplitude, $\hat{U}$, from the AIRS observed temperature amplitude using the polarization relation. This is required as an input to GROGRAT.

$$\hat{U} = \frac{g}{N}\frac{T'}{\bar{T}}\left[1-(f/\hat{\omega})^2\right]^{-1/2} \tag{6}$$

We output the ray location (i.e., latitude and longitude) at 1 km altitude increments, tracing the ray downward from 39 km until the ray terminates. Typically, GROGRAT terminates rays because (a) the ray has reached the bottom of the prescribed atmosphere, (b) the ray has reached a critical level and stalls vertically (i.e., has a vertical velocity <0.01 ms^{-1}) and a small minority of rays terminate due to (c) vertical reflection which is not supported by GROGRAT. This means that waves will not only sometimes terminate at their source but can also be traced backward through the source without terminating. Unfortunately, this means that rays can travel to the ground but the real source of the wave could lie somewhere along the raypath (Preusse et al., 2014). In our results, we find that 61% of all rays terminate because they have reached the ground; this percentage will be a combination of correctly traced orographic waves as well as rays that have been back-traced through non-orographic sources and continued downward to the ground. The height at which the ray terminates is referred to as the lowest traceable altitude (LTA). Finally, it is important to note that this method is not perfect. Rays may be mis-traced, which we define as meaning that the path the ray takes deviates from the real path of the GW in the real atmosphere. This can happen for several reasons. First, inaccuracies in determining GW properties, which can arise from instrument noise/errors in the observation of GWs or due to the approximations made when calculating GW properties from these observations. Second, inaccuracy of ERA5 background wind fields will affect both the ground-based phase speed determination and the tracing itself, either due to differences in the reanalysis compared to the real atmosphere (particularly in the stratosphere where reanalysis is not well constrained by observations) and by our simplifying assumption that the rays trace through a static (in time) background atmosphere.

Figure 2 demonstrates our method as applied to an example swath of AIRS data, recorded on 4 June 2010 at ~04:00 UTC. Panel (a) shows temperature perturbations at 39 km altitude, and panel (b) shows the areas identified by our masking technique as GWs. Panel (c) shows the rays we backward trace from these waves; the rays are shown as green lines, and one has been initialized from each pixel of AIRS data at 39 km.

In this example, most rays terminate because they reach the bottom of the specified background (2 km altitude): one group of rays travels almost directly downward toward the Antarctic Peninsula (approximately 65°W, 65°S), whereas another traces back to the Southern Andes, possibly due to refraction in the jet (Dunkerton, 1984; Geldenhuys et al., 2023; Sato et al., 2011; Wright et al., 2017). The raypath toward large mountain ranges and all the way down to 2 km suggests that the orography is the likely source of these GWs.

3.3. Post-Processing of Traced Rays

Backward ray-tracing five months of detected waves from all AIRS data during May–September 2012 results in 14.2 million rays, which we then analyze in a number of different ways. We first investigate the meridional propagation of GWs by considering the difference between their observed latitude (i.e., the latitude at which they are observed by AIRS at 39 km altitude and where a ray is initialized) and the latitude the ray is then traced back to lower in the atmosphere. This provides an estimate of the meridional propagation distance of the waves.

Second, we investigate the propagation of GWs from specific orographic sources: the Southern Andes, Antarctic Peninsula, Prince Charles Mountains, Transantarctic Mountains, South Georgia, and Kerguelen (Figure 1). To do this, we consider all the rays that are traced back to chosen regions with an LTA of <5 km and explore how far away these waves are observed in the stratosphere by AIRS.

Third, we divide waves that are traced to land and ocean and present the observation location and respective momentum fluxes from these two classes. This quantifies the proportion of MF traced to land and ocean, providing an estimate of the split between orographic and non-orographic GW activity to the observed stratospheric MF in this region. This is an upper estimate of orographic activity as sources over land may also be non-orographic. We examine the split spatially in monthly averages and temporally in the zonal mean momentum fluxes. We note that due to AIRS' polar orbit, we have more observations and hence initialize more rays at high latitudes. To compensate for this effect, in this work we consider daily mean results of MF as almost the whole area poleward of 30°S is observed by AIRS at least once per day.

Finally, we further divide the geographical regions (including small islands) and quantify GWs traced back to different areas and weighted by their daily mean observed stratospheric MF. This quantifies the proportion of observed MF in the stratosphere that is traced back to each region. A key point here is that we do not claim this represents all MF originating from each region: we explicitly only trace rays that are observed by AIRS in the stratosphere. Hence, these waves must have been able to propagate up to these altitudes without dissipating or getting removed via critical level interactions.

4. Results

4.1. AIRS Observations and Background Winds

Figure 3 shows AIRS observations of GWs and ERA5 zonal winds at 39 km altitude. The left column shows the total number of GWs observed each month. In the middle column, we scale these totals by the number of AIRS overpasses to give an occurrence frequency.

Both GW metrics show localized hotspots, as well as general activity over the Southern Ocean up to ∼20°S. Overall, GW activity increases from May until mid-winter (July and August) before tailing off. This seasonal peak agrees with and is likely to be related to the background wind structure, which also peaks in strength in mid-winter. It is well-known that the Southern Andes act as the largest individual source of GW activity in this region and arguably the whole Earth system, as first identified by Eckermann and Preusse (1999), confirmed with AIRS (Hindley et al., 2020; Hoffmann et al., 2013), Global Positioning System Radio Occultation (GPS-RO) (Hindley et al., 2015), the SABER, MLS, and HIRDLS limb sounders (Alexander et al., 2008; Ern et al., 2018; Geller et al., 2013; Wright & Gille, 2013; Wright et al., 2016; Wu & Eckermann, 2008), and the Aeolus Doppler wind profiler (Banyard et al., 2021). Other orographic GW hotspots can also be seen in our data, including the Antarctic Peninsula, South Georgia, Kerguelen, the Prince Charles Mountains, the Transantarctic mountains, Tasmania, and New Zealand. We see GW activity downstream of orographic sources, particularly from the Southern Andes and Antarctic Peninsula extending into the Drake Passage. We also see GW activity over the open ocean away from clear orographic sources. The exact sources of these GWs remain unclear and difficult to attribute. Finally, the observed GW activity clearly shares key morphological features with the zonal wind field at the same height, presented in the right column. The polar night jet sits above the Southern Ocean during all five months, maximizing in strength at ∼80 ms^{-1} in July. Observed GW activity follows the jet center, and a stronger jet correlates spatially and temporally with stronger GW activity. This is due to (a) refraction to longer vertical wavelengths, which increases visibility to AIRS and (b) actual geophysical lateral propagation of GWs into the center of the jet, which has been shown in observations, for example, (Hindley et al., 2015, 2020; Wright et al., 2017) and is discussed in the next section below.

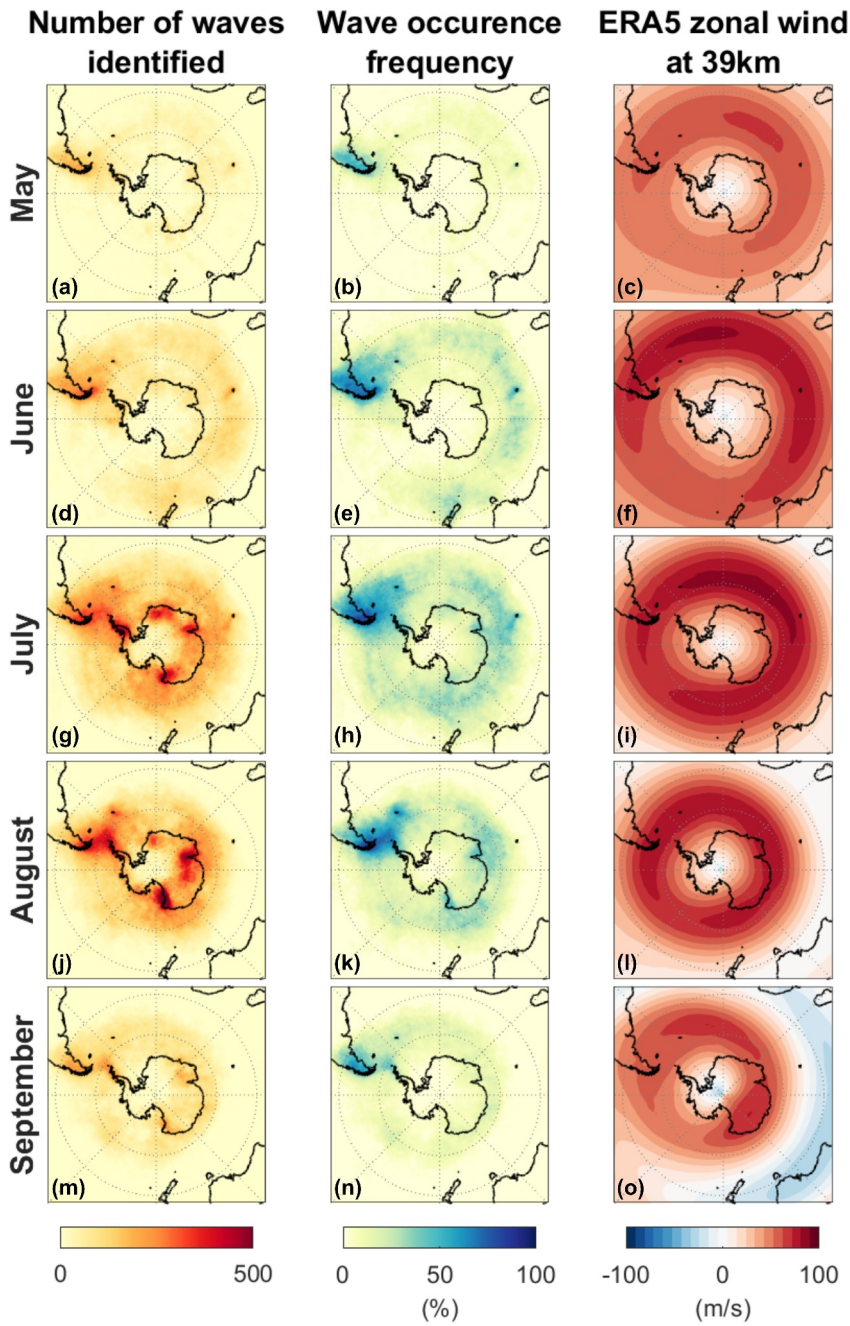

Figure 3. AIRS observed GWs and ERA5 background winds. Left column, the total number of GW observations at 39 km altitude from AIRS. Middle column, GW occurrence frequency at 39 km from AIRS calculated from number of waves identified per overpass. Right column, ERA5 zonal winds at 39 km. Rows are different months, (a–c) May, (d–f) June, (g–i) July, (j–l) August, and (m–o) September.

4.2. Focusing of Gravity Waves Toward 60°S

Numerous studies have hypothesized that a significant proportion of the "missing" MF at 60°S in chemistry-climate models reaches 60°S via meridional focusing (Geller et al., 2013; Hindley et al., 2015; McLandress et al., 2012; Moffat-Griffin et al., 2020; Strube et al., 2021; Wright et al., 2017; and others). In particular, persuasive evidence has been shown of orographic waves from the Southern Andes and Antarctic Peninsula converging in this way. In a numerical modeling study, Sato et al. (2011) used the high vertical resolution Kanto model (Watanabe et al., 2008) to show that rays launched from the surface of the Andes and Peninsula would be

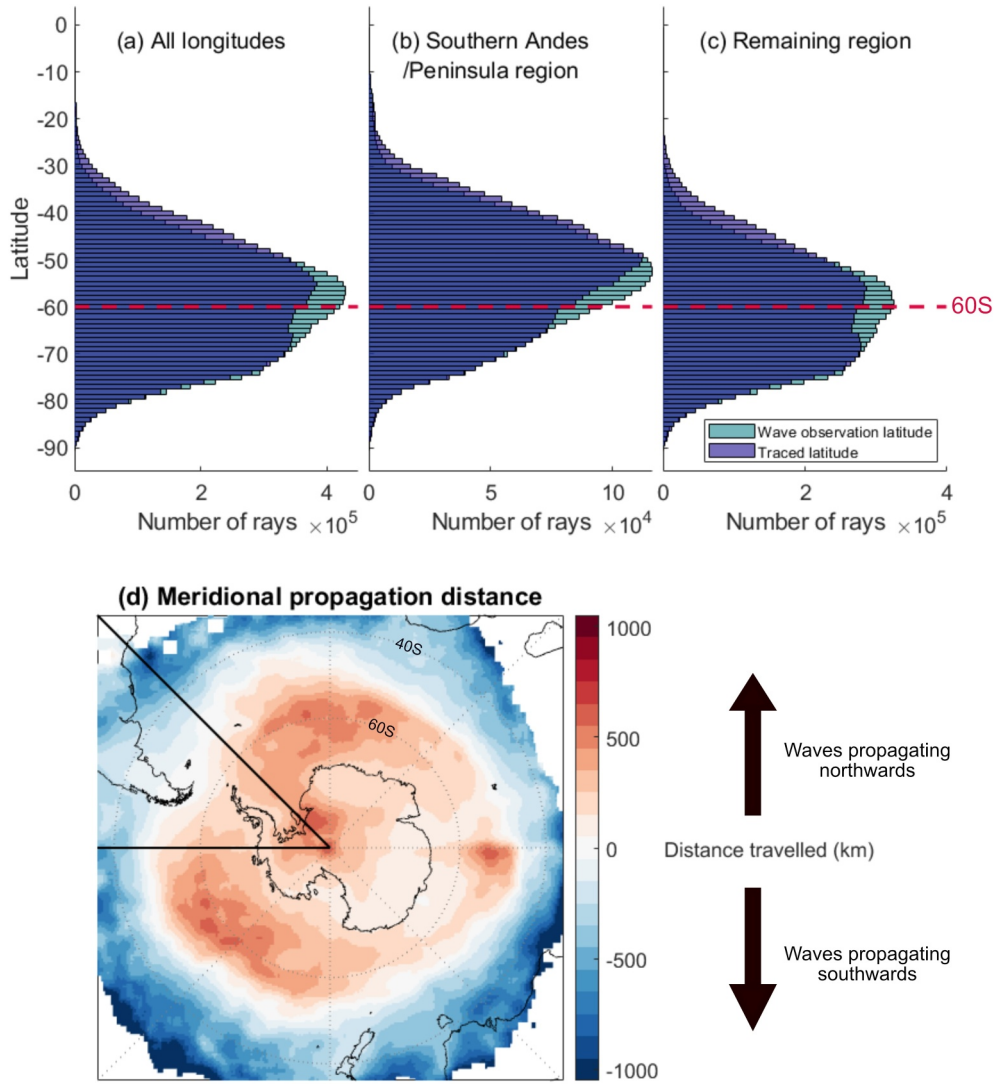

Figure 4. Meridional propagation of rays. Panels (a)–(c) show histograms of the observation and traced latitude of the waves. We define the GW "observation" latitude as the latitude that AIRS observes at the GW at 39 km, and the "traced" altitude as the lower-altitude latitude which the ray traces back to. Panel (c) shows all longitudes, panel (b) just the Southern Andes and Antarctic Peninsula region (90°W-30°W), and (c) the remaining regions. Panel (d) shows the average meridional distance traveled by the rays in km positioned by the traced position of the ray (i.e., the source location of the GW) and the black lines denote the region divide for panels (b) and (c).

expected to exhibit this focusing, while observationally, Hindley et al. (2015) demonstrated that GW potential energies derived from GPS-RO measurements showed evidence of this focusing southward from the Southern Andes, but did not find evidence for northward propagation from the Peninsula using data from 2010. Wright et al. (2017), meanwhile, used instantaneous AIRS-observed group speeds over the Drake Passage to infer, focusing from both the Andes and the Peninsula based on the observed wave orientation. They found that the orientation of the waves turn in the wind, demonstrating that the refraction of the waves in the background winds plays a role in their lateral propagation.

To investigate this, we first compare the start and end locations of our 14.2 million rays as a function of latitude. Figure 4a shows the results of this analysis as a pair of overlaid histograms. For clarity of discussion, we define the GW "observation" latitude as the latitude that AIRS observes at the GW at 39 km, and the "traced" altitude as the lower-altitude latitude, which the ray traces back to. The observation-level distribution of waves, shown in cyan, forms a near-Gaussian distribution centered around 55°S, consistent with Figure 3. The traced latitude (dark blue),

however, produces a bimodal distribution, with a local minimum at ∼60–65°S. This suggests that the GWs seen by AIRS around the Southern Ocean are largely generated by sources, north and south of where they are observed in the stratosphere. The peak centered at 55°S is larger than the peak centered at 70°S, suggesting that sources to the north play a slightly larger role in the observational-level peak near 55°S. The same histogram as panel (a) but restricted by observation latitudes between 55°S and 65°S can be found in the Supporting Information (Figure S1 in Supporting Information S1). Panels b and c present this distribution for a subset of longitudes, panel b is the Southern Andes/Antarctic Peninsula region (90°W-30°W) and is shown as the black lines in panel d. Here we see that the observed latitudes peak near 50°S to 55°S, which is over the southern tip of the South American continent. Traced latitudes appear to be shifted further northward with a small local maximum near ∼60–65°S coinciding with the tip of the Antarctic Peninsula. Panel c shows the remaining longitudes with the peak observation location near 55°S to 60°S and a much clearer bi-model distribution in the traced latitudes. This suggests that the GW activity from the Southern Andes dominates and skews the observed distribution northward. These three histograms are consistent with the focusing of GWs, on average, toward the Southern Ocean.

Figure 4d characterizes how far these rays propagate meridionally. Specifically, we show the difference between the observation latitude and the traced latitude. Positive values (red) indicate that, on average, waves have propagated northward from their source to the observation altitude, while negative (blue) values indicate that waves have propagated southward. We see northward propagation over the Antarctic continent and near-continental regions of the Southern Ocean and southward propagation from more equatorward regions of our map. We find local minima over and near orographic sources of GWs (the Southern Andes, the Antarctic Peninsula, South Georgia, Kerguelen, and New Zealand), which is likely due to the high frequency of wave events. Equally, regions which show a local maxima of lateral propagation distance typically have lower GW activity.

Over Antarctica, waves generally propagate ∼200–600 km northward, traveling outwards over the Southern Ocean into the jet core. Over the ocean itself, meanwhile, meridional wave propagation averages out between north and south. Further north, our results suggest that waves can propagate meridional distances as large as 1,000 km from source to observation; however, in practice the number of waves seen here is small and hence inaccurate traces may contribute significantly to this mean.

This result is the first time focusing over the Southern Ocean has been demonstrated across all longitudes of the Southern Ocean by backward ray-tracing observations, providing a vital quantitative constraint on the average distance traveled by these waves. This suggests that on average, all GWs, both orographic and non-orographic, converge toward and that both may contribute significantly to the missing MF near 60°S. The significance of this result is that it expands on previous conclusions of the modeling study of McLandress et al. (2012), who focused on orographic waves but concluded that a significant non-orographic contribution was unlikely. It does however, agree with the observational work of Hindley et al. (2016) and Holt et al. (2017), who used AIRS observations and found that directional MF (in Hindley et al., 2016) and wave propagation direction (in Holt et al., 2017) visible to AIRS converged toward 60°S at all longitudes.

Our results apply only to GWs within the observational filter range of AIRS. However, we can make inferences about other parts of the observational filter from work using other data sets. Specifically, Moffat-Griffin et al. (2020) carried out a comprehensive study of GWs observed by radiosondes launched from 11 different sites in Antarctica, the Southern Andes and from small islands in the Southern Ocean. They calculated the angular distribution of MF for 12–30 km altitude and found that for sites poleward of 60°S, the MF was northward and for sites at lower latitudes, the MF was southward. This again suggests a focusing of GWs over the Southern Ocean in agreement with our results. The observational filter of radiosondes and AIRS observations do not overlap (Alexander et al., 2010; Wright et al., 2016), radiosondes are capable of observing waves at the shorter vertical wavelengths that AIRS cannot see. We note that this lateral focusing effect is more likely to be greater for the short vertical wavelengths observed by radiosondes since the accumulated amount of lateral refraction of horizontal wavenumbers due to lateral shear depends on the amount of time wave groups reside within these lateral shear zones, which will be longer in general for short vertical wavelengths of slower vertical group velocity. This suggests that our results may generalize across the GW spectrum. This radiosonde data set may also cover some of the same waves we trace from AIRS at 39 km, but at lower wind velocities at lower altitudes.

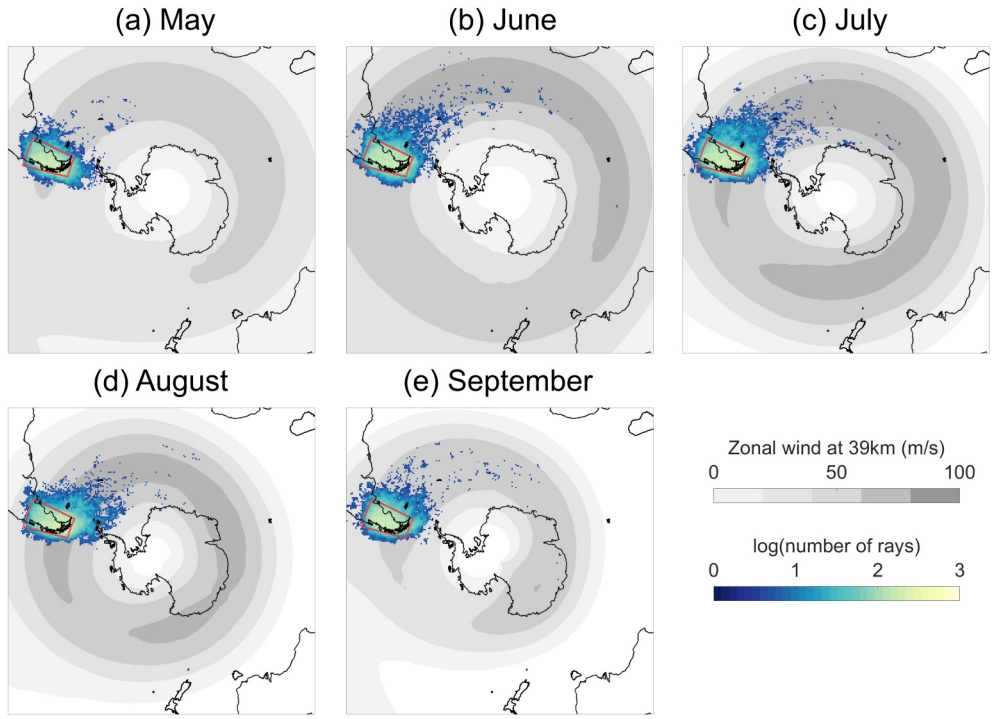

Figure 5. The observation location of all rays traced back to the Southern Andes. Color graduation denotes the number of rays traced back to the red box (log10 scale). Gray contours show the ERA5 eastward wind at 39 km. Panels show different months, (a) May, (b) June, (c) July, (d) August, and (e) September.

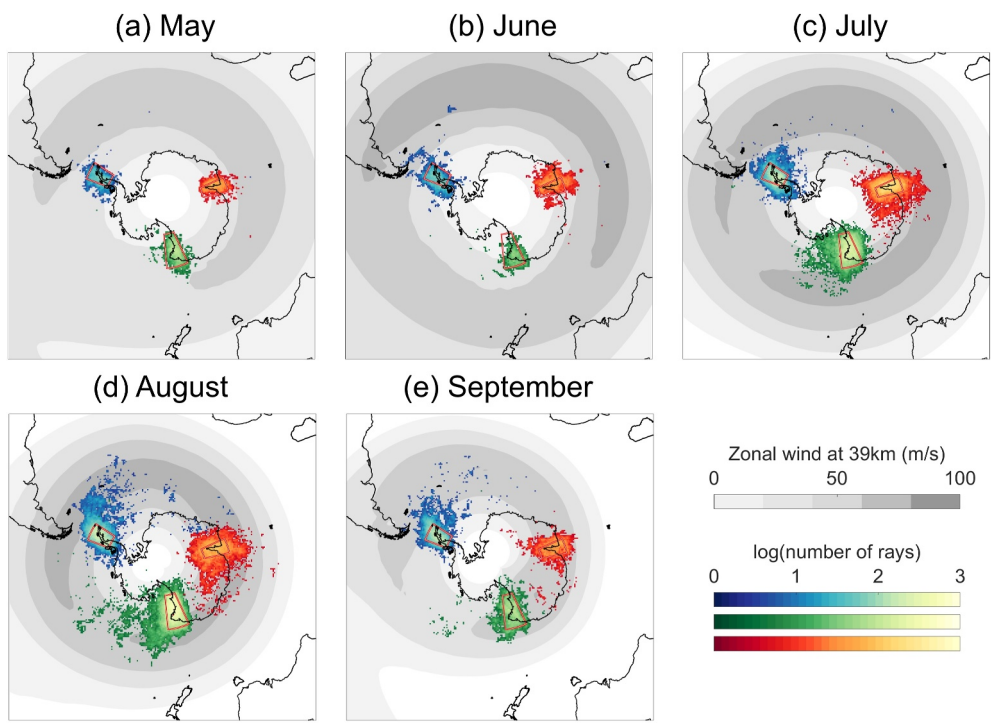

Figure 6. The observation locations of all rays traced back to key orographic source regions on the Antarctic Continent. Color graduation denotes the number of rays traced back to each red box (log10 scale). The Antarctic Peninsula (blue), Transantarctic Mountains (green), and the Prince Charles Mountains (red). Gray contours show the ERA5 eastward wind at 39 km. Panels show different months, (a) May, (b) June, (c) July, (d) August, and (e) September.

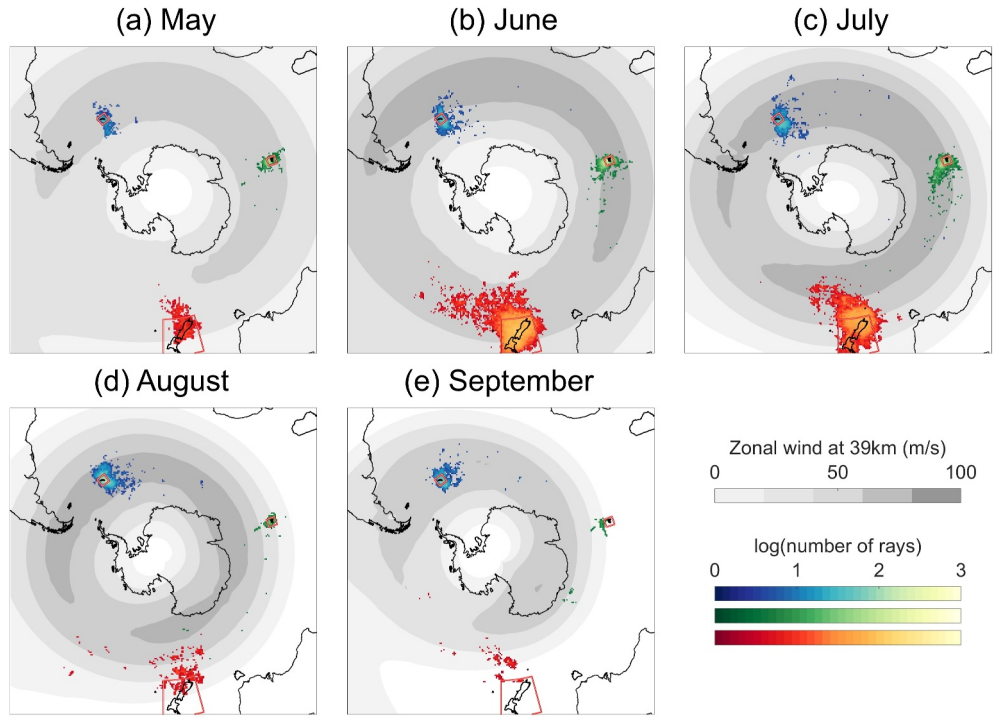

Figure 7. The observation locations of all rays traced back to key island source regions. Color graduation denotes the number of rays traced back to each red box (log10 scale). South Georgia (blue), Kerguelen (green), and New Zealand (red). Gray contours show the ERA5 eastward wind at 39 km. Panels show different months, (a) May, (b) June, (c) July, (d) August, and (e) September.

4.3. Lateral Propagation of Orographic Gravity Waves

We next explore the horizontal propagation of GWs from orographic sources. We do this by considering all rays that trace back to defined regions over orography and which terminate at altitudes less than 5 km. This is shown in Figures 5–7; here, colors show the number of rays traced back to each region, with the ERA5 westward wind at 39 km shown in greyscale. Figure 5 shows the Southern Andes (blue), Figure 6 shows the Antarctic Peninsula (blue), the Prince Charles Mountains (red) and the Transantarctic Mountains (green), and Figure 7 shows South Georgia (blue), Kerguelen (green) and New Zealand (red). These regions were selected from the hotspots found in Figure 3.

In Figures 5–7, we see that the overwhelming majority of waves are observed directly above the region that they trace back to. This suggests that the majority of the AIRS-observed waves travel almost directly upward. AIRS is particularly sensitive to long-vertical-wavelength waves, which tend to have fast vertical group velocities and thus are expected to behave in this way. Despite this, in all cases we see trails of waves propagating downstream from each orographic region. This is particularly clear for the Southern Andes (Figure 5), where GWs observed hundreds of km downstream can be traced back to <5 km altitude here. This is consistent with Sato et al. (2011), their Figure 5, who launched waves from the Southern Andes and Antarctic Peninsula with horizontal wavelengths of 300 km and a ground-based phase speed of zero through idealized background conditions. These rays propagated laterally up to 50° eastward before reaching 40 km in altitude. The SOUTHTRAC-GW campaign which comprehensively explored GW dynamics over the Andes with airborne observations and high-resolution modeling found compelling evidence of refraction of GWs into the polar night jet and subsequent eastward propagation toward 60°S (Geldenhuys et al., 2023; Rapp et al., 2021). Recently, Krasauskas et al. (2023) investigated the oblique propagation of GWs over the Southern Andes in a multi-instrument case study using GLORIA measurements at 8–15 km altitude and observations from the Airborne Lidar for Middle Atmosphere research (ALIMA) at 20–80 km in height. In a case study in September 2019, they used forward ray-tracing from GLORIA inputs and compared traced ray properties to ALIMA observations. This allowed them to directly observe horizontal refraction of orographic GWs in the strong stratospheric winds. Ehard et al. (2017) also

observed horizontal refraction of a large-amplitude mountain wave event using ground-based lidar observations from New Zealand, ray-tracing, AIRS observations and ECMWF data. This study highlights that propagation pathways and ability of waves to reach the stratosphere are strongly dependent on the background winds.

Recently, Rhode et al. (2023) devised a mountain wave model for quantifying the horizontal propagation of orographic GWs. This model is based on identifying ridges from topography data, determining GW launch parameters then forward tracing waves from the mountains to predict MF at higher altitudes. Comparison with HIRDLS satellite data from 2006 showed promising agreement, validating their model. Their predicted GW activity, in particular the downstream propagation patterns agree well with the findings of our study, wakes of GW activity are found downstream of the Southern Andes, Kerguelen, Tasmania, and New Zealand of similar shape, which also peak throughout June and July. In our results for the Antarctic regions, the peak month is August which differs from Rhode et al. (2023); however, this may be due to differing background wind conditions across different years. This mountain wave model was implemented in a parametrization which redistributes GW MF horizontally by Eichinger et al. (2023) and they found a reduction in model biases as a result. This agreement between the mountain wave model (Rhode et al., 2023) and our findings here, as well as an improvement in model biases (Eichinger et al., 2023) shows a promising pathway to improving GW parametrizations.

Throughout all months, in agreement with Figure 4, we also see orographic waves converging over the Southern Ocean. It is especially clear in August, where waves from the Andes propagate south-east (Figure 5d) and waves from the Peninsula north-east (Figure 6d) between surface and the stratosphere. In June and July, we also see waves traced back to Kerguelen from south-east of the island (Figures 7b and 7c), that is, propagating into the jet.

The propagation pathways of our traced GWs vary significantly by region and by month, which we attribute primarily to stratospheric background wind variability. The strong jet biases our observations of stratospheric GWs in two ways: (a) the strong westerly winds preferentially allow westward propagating GWs to propagate to observation levels (Hindley et al., 2016) and (b) GWs are refracted to longer vertical wavelengths in the strong winds, making these waves more observable by AIRS (Hindley et al., 2019). The first of these effects acts as a real control on the MF present in the system; however, the second acts on our results as an observational bias. The variation of GW activity with the background wind is consistent with the results of Hoffmann et al. (2016), who correlated AIRS-observed orographic GWs separately with (a) surface winds and (b) stratospheric winds, and found that observation-level winds exhibited a much higher correlation with GW activity, which they attributed to observational filter effects. Hendricks et al. (2014) also explored correlations between stratospheric GW activity and background winds in ERA-interim analysis. They found that stratospheric GW activity measured by absolute divergence at 5 hPa in a boxed region over the Andes positively correlated with the 700 hPa zonal wind particularly in June and July.

We also see that regions of stronger wind correlate with longer wakes of GW activity downstream of orographic sources. This is particularly clear over Kerguelen: the GW wake here is most prominent in July (Figure 7c). The increased wind speed with altitude refracts GWs to longer vertical wavelengths which would then increase their likelihood of observation by AIRS and possibly explain these extended downstream wakes. However, this is counterbalanced by the increase in vertical wavelength meaning that a wave would then tend to propagate more vertically. GWs originating over New Zealand also exhibit this effect in May (to some extent), June and July (Figures 7b and 7c), when the jet reaches further north. The activity of the polar night jet provides a plausible mechanism for the high level of GW intermittency seen over Kerguelen and New Zealand in studies such as Wright et al. (2013).

Waves traced back to South Georgia exhibit a ship-wave pattern with two downstream wakes, one to the north-east and another to the south-east. A similar wave pattern was observed in both AIRS observations and the Met Office Unified Model in Hindley et al. (2021). This wave pattern is found over isolated islands, such as Auckland Eckermann et al. (2016), where the background winds allow waves to propagate upward with both northward and southward directions without preference. Kerguelen is another isolated island and also produces this pattern when the background wind conditions allow it (Figure 7c, for example); however, most of the time, Kerguelen lies north of the jet, and hence we do not observe the ship-wave pattern here.

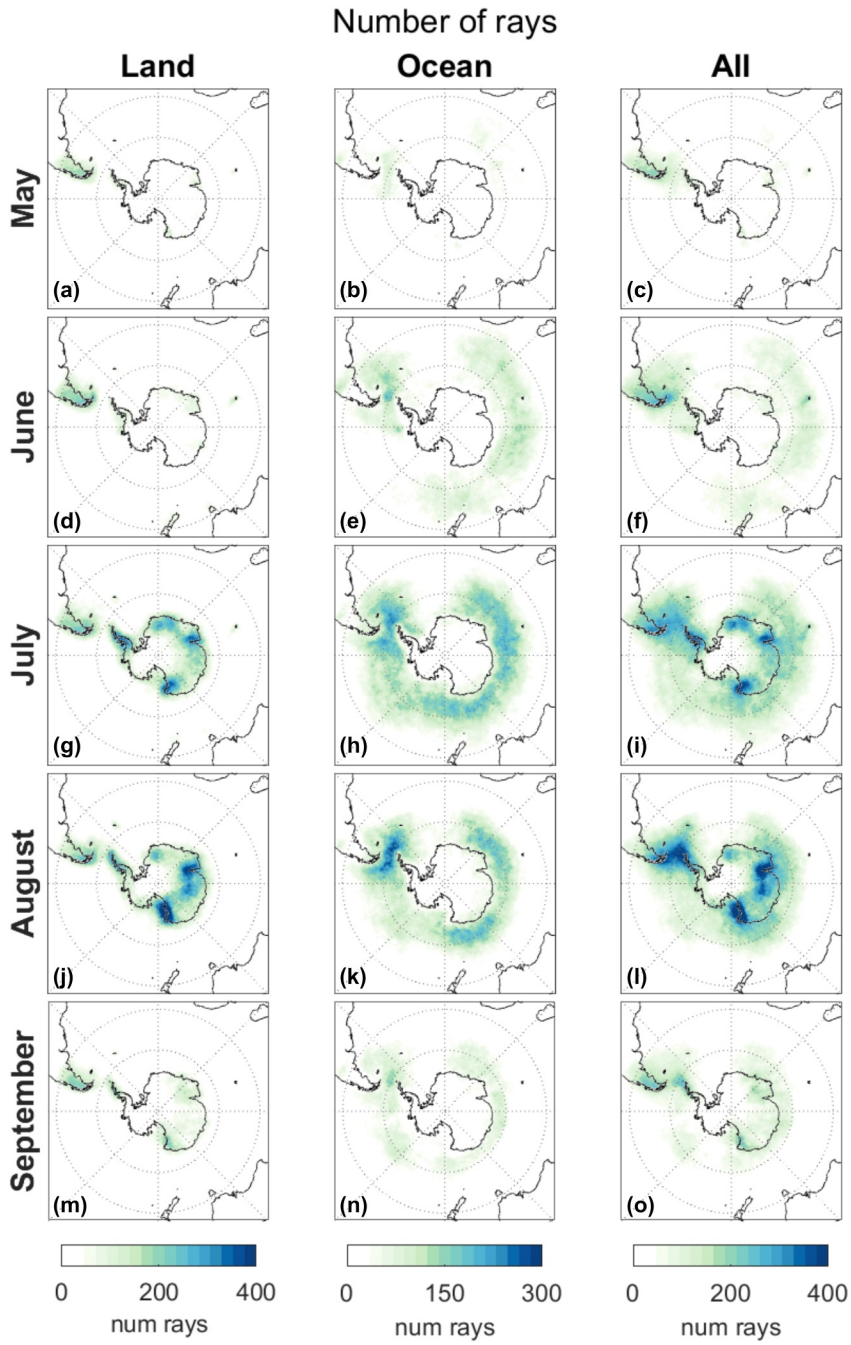

Figure 8. Number of rays traced back to land (left column), ocean (middle column) and combined (right column), positioned by the observation location of the ray. Rows are different months, (a–c) May, (d–f) June, (g–i) July (j–l), and (m–o) September. Note that the same figure with a logarithmic colorscale can be found in the Supporting Information (Figure S2 in Supporting Information S1).

4.4. Orographic and Non-Orographic Sources of Gravity Waves

We next use our traced rays to separate the observed GWs into those that are traced back to land (defined as land areas plus an extra 200 km coastline) and those that trace to the ocean. Figure 8 shows the mean number of rays traced to land (left column), sea (middle column) and total for each month. Figure 9 presents the same division of rays weighted by the observed stratospheric MF of each ray. We calculate the monthly average from daily mean values to correct for the polar orbit of AIRS (as all regions presented are observed at least once every 24 hours).

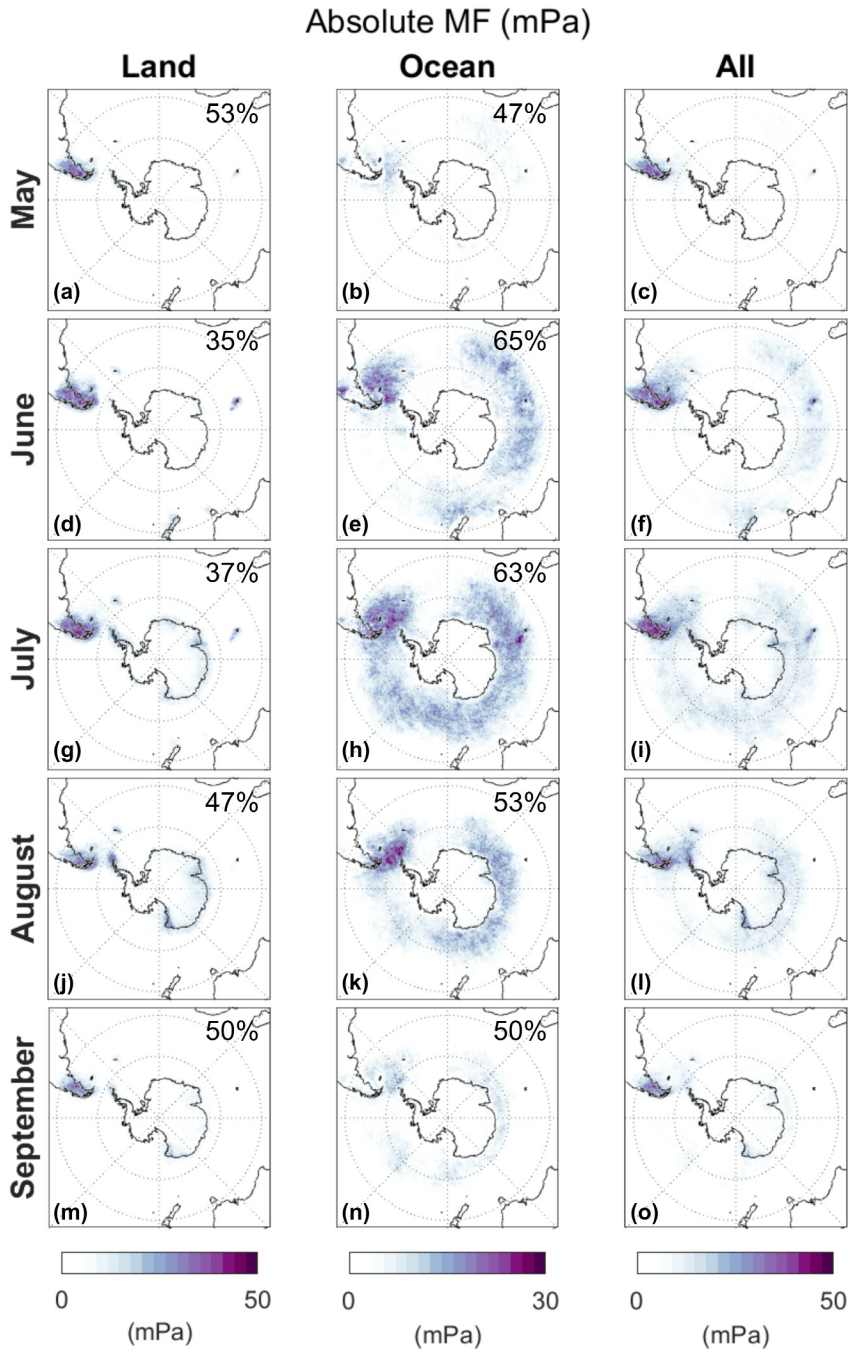

Figure 9. Stratospheric absolute momentum flux (mPa), as measured by AIRS, of rays traced back to land (left column), ocean (middle column) and combined (right column), positioned by the observation location of the ray. Rows are different months, (a–c) May, (d–f) June, (g–i) July, (j–l) August, and (m–o) September.

Wakes of GW activity is found downstream of small islands, in both the number of rays (Figure 8) and MF (Figure 9). In particular, downstream of Kerguelen and Heard Island (a small island to the south-west of Kerguelen, 53°S 73°E) in July (Figure 9g) we see a large downstream wake of rays with significant MF that traces back to land (Figures 8j and 9j). This is consistent with the results presented in Figures 5–7.

We previously discussed the propagation and behavior of orographic GWs in Figures 5–7. Here we focus our discussion on the waves that do not trace back to land (middle column of Figures 8 and 9); these exhibit some

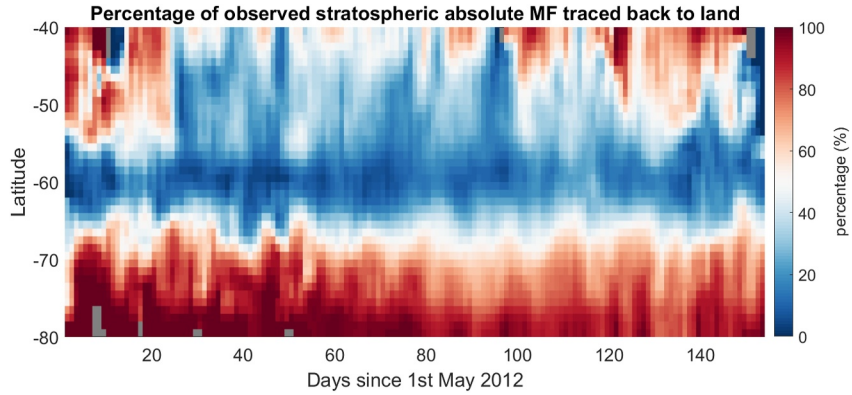

Figure 10. Percentage of zonal-mean stratospheric absolute momentum flux, as measured by AIRS at 39 km altitude, traced back to land regions. *y*-axis is latitude and *x*-axis is days since first May 2012. Gray patches denote where there is no observed GW activity.

interesting results. First, there is a surprising peak of GW activity in the Drake Passage between the Southern Andes and the Antarctic Peninsula. This feature is present throughout all months but is perhaps most evident in mid-winter (Figures 8 and 9, panels e, h, and k). This suggests that a significant number of waves are observed in the Drake Passage and not traced back to orography. Considering the number of rays (Figure 8, panels e, h, and k), we see that the Drake Passage is dominated by a high number of wave observations that are traced back to the sea. However, in the associated absolute MF of this region (Figure 9, panels e, h, and k), we see a pattern of higher MF only to the south-east of the tip of the South America and downstream from there. The fact that we see a similar number of rays around the Drake Passage but that only those downstream of the Andes carry larger momentum fluxes suggest that the land plays a role. We have three possible hypotheses for the increased wave activity in the Drake Passage, which may all contribute to some extent. (a) High MF orographic GWs from the Southern Andes and Antarctic Peninsula which have propagated downstream that are mis-traced by the backward tracing. (b) Waves generated by storms funneling through the Drake Passage, and (3) GWs generated by an orographic-jet mechanism. Geldenhuys et al. (2021) presented the first observational evidence of such orographic-jet generation using GLORIA observations from a campaign over Greenland. They describe how orography modifies the wind flow over large scales, resulting in an "out of balance jet" which then excites GWs.

In Figure 8k, we see that there are also hotspots of waves that trace back to the ocean offshore of the Prince Charles Mountains and the Transantarctic mountains (in addition to those previously discussed around the Drake Passage). The existence of these hotspots near these orographic suggests that our hypotheses (1) and (3) may be perhaps more likely. However, we note that in the figure of associated MF, Figure 9k, the MF associated with the Drake Passage is far higher than the Prince Charles Mountains and the Transantarctic mountains, suggesting that we cannot discount additional wave generation sources in the Drake Passage such as storms. There are also small hotspots of MF downstream of Kerguelen and South Georgia and also near the Transantarctic Mountains and the Price Charles Mountains, which trace back to the sea (Figure 9). These are visible in the absolute MF of waves, which are traced back to the sea (June and July, Figure 9-middle panels), suggesting that hypotheses (1) and (3) play a role here also.

Another feature of the waves traced back to sea is the hotspot of activity over the ocean, stretching from the south of Africa (≈30°W) clockwise around the Antarctic continent (this is seen in Figures 8 and 9 in panels e, h, and k). This activity does not circle the entire continent, there is a clear gap between South Georgia and near the southern tip of Africa. Some studies such as Wei et al. (2022) who studied GW MF from ECMWF experiments report on a continuous stretch of wave activity in this region without the gaps presented in this study. However, similar gaps (although less pronounced) have been reported in AIRS observations by Holt et al. (2017) and Hindley et al. (2020), suggesting that the gaps could be a product of the AIRS observational filter or AIRS processing method.

Figure 10 shows the percentage of total zonal-mean observed stratospheric MF (at 39 km altitude) that is traced back to land. The remaining percentage consists of MF that is traced back to the ocean. This provides an estimate on the relative proportion of orographic and non-orographic MF in the stratosphere at each latitude. This is also

Table 1
Percentage of Monthly Stratospheric Absolute Momentum Flux (Observed by AIRS at 39 km Altitude) Traced Back to Land

	May	June	July	August	September	Average
40–45S	60%	40%	46%	59%	66%	54%
45–50S	47%	31%	31%	41%	54%	41%
50–55S	42%	29%	25%	31%	39%	33%
55–60S	21%	16%	15%	19%	18%	18%
60–65S	24%	17%	21%	27%	24%	22%
65–70S	62%	53%	50%	52%	56%	55%
70–75S	83%	83%	72%	72%	75%	77%
75–80S	96%	96%	86%	87%	86%	90%

Note. Rounded to 2 significant figures.

quantified as monthly mean for 5 degree latitude bands in Table 1. From Figure 10 we see that northward of 50°S orographic sources dominate at times; however, non-orographic sources make up the majority of MF from days 25 to100 (late May to early August). Poleward of 70°S, the majority of the area is covered by the Antarctic continent and we see that the majority of flux is traced to land. Around 60°S itself, non-orographic sources dominate, with the contribution from orography, on average, around 20%, increasing to as much as ∼35% around day 115, decreasing to as low as ∼5% near day 45. There is very little land mass at 60°S itself, Coronation Island (60.6°S 45.4°W) off the tip of the Antarctic Peninsula is the largest island at this latitude. This suggests, in line with our previous results, that this orographic contribution to the observed stratospheric MF is the result of meridionally propagating waves. At the same time this also highlights that the majority of the MF observed at 60°S has non-orographic sources. A proportion of this will be due to the high momentum fluxes traced to the Drake Passage region, possible mechanisms for which we discussed previously. However, this does highlight the importance of non-orographic sources around 60°S.

Non-orographic sources have not been explored in detail in previous studies; however, Hendricks et al. (2014) suggests that stratospheric GW activity may be attributable to storms. Holt et al. (2017) investigated absolute MF from a high-resolution GEOS5 Nature Run in relation to both precipitation and frontogenesis. They found that fronts and precipitation were weakly correlated with absolute MF between 30°S-80°S at most longitudes, although correlations were higher at the lower latitudes. Plougonven et al. (2017) explored the relationship between wind speeds and GWs in the lower stratosphere in a mesoscale model (which would not suffer from the observational filter problem that observations do) and found that large values of non-orographic MF was more likely in regions of strong winds. They suggest several possible reasons for this, including spatial variations in tropospheric sources, lateral propagation, local generation of GWs in the stratospheric winds or vertical wind shear. More recently, Green et al. (2024) calculated momentum fluxes from Project Loon superpressure balloon data. They analyzed the relationship between zonal momentum fluxes in the lower stratosphere (16–21 km altitude) and zonal background winds over the Southern Ocean (excluding orographic regions), and found increasing MF with increasing background winds which they argued are due to a combination of wave sources and filtering.

Strube et al. (2021) also investigated a case study over New Zealand and used backward ray-tracing to evaluate propagation paths and sources of GWs in the ECMWF-IFS model from 25 km altitude. A strength of this study is in the self-consistency of tracing ECMWF waves through the ECMWF background atmosphere, thereby reducing the likelihood of waves being mis-traced. They found that first, stratospheric GWs are subject to far lateral displacement, in strong agreement with the results of our study (Section 4.2 and 4.3). Second, their source attribution revealed that both non-orographic and orographic sources are important in the region around New Zealand and corroborates the findings in our work that non-orographic waves can originate over the open ocean. Recently, Gupta et al. (2024) carried out a different case study over the Southern Andes in ERA5 reanalysis and two high models (a 1 km run of the IFS and the coarser EMAC model). They found significant fluxes away from the Andes, suggesting that there are major contributions from non-orographic sources in this region. This model-based study supports our findings in the importance of non-orographic sources.

In future work using this ray-traced data set we aim to better quantify the source mechanisms of non-orographic GWs, particularly the puzzling enhancement in the Drake Passage region.

4.5. Momentum Flux From Different Source Regions

We next quantify the fraction of observed stratospheric MF which traces back to specific geographic regions, illustrated in Figure 11a. These regions are defined as follows:

- We first split Antarctica into three regions, specifically an East Antarctic region from 0°-135°E, an Antarctic Peninsula region from 135°W-0°, and an Transantarctic region from 135°E-135°W.

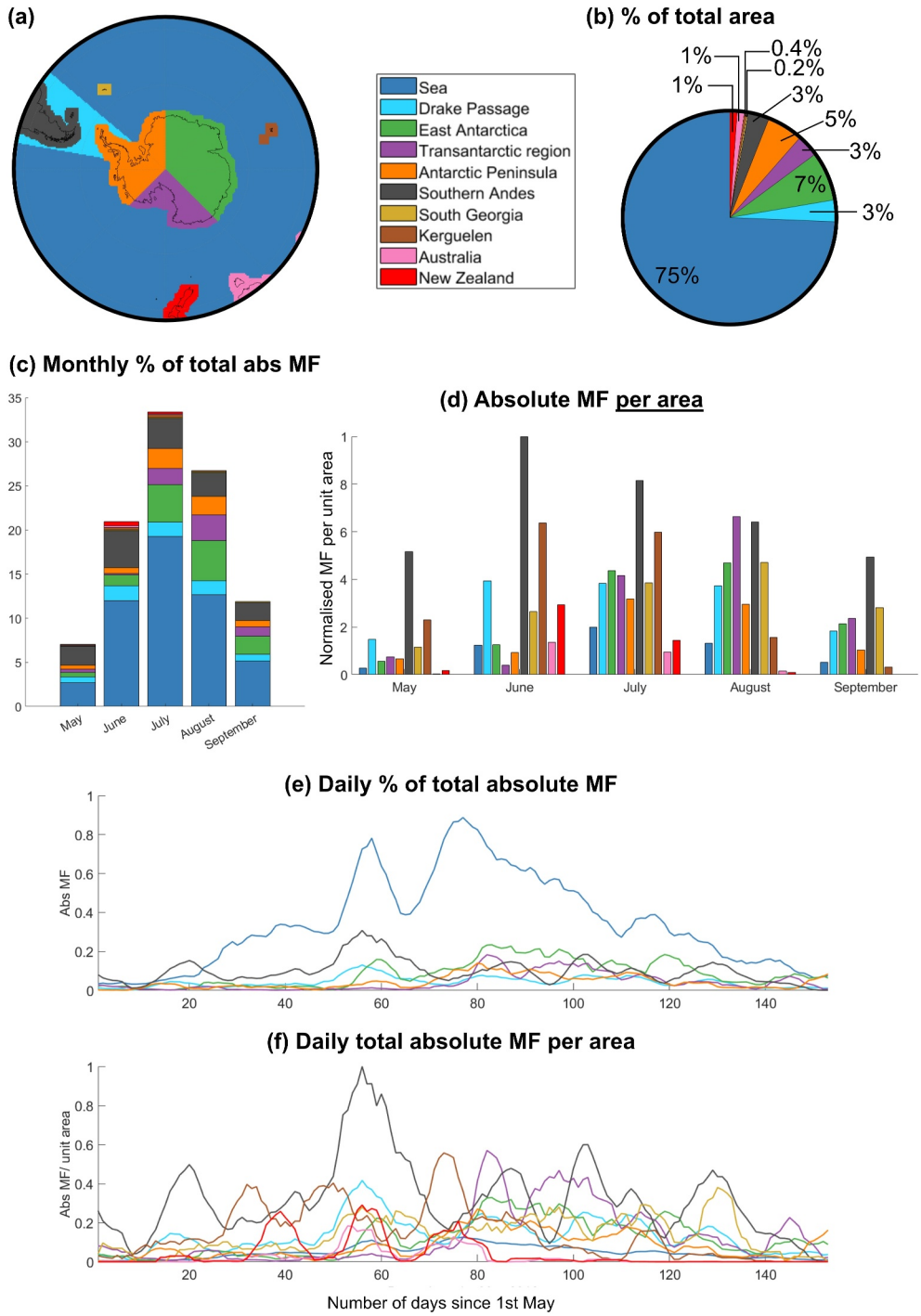

Figure 11. The proportion of absolute stratospheric momentum flux (MF) (observed by AIRS at 39 km altitude) traced back to different regions. Panel (a) shows the different regions. Panel (b) shows the fraction of the total area that each region makes up, (c) shows the percentage of total flux split per month and per region, and (d) shows the same absolute MF scaled by the area of each region. Panel (e) shows the daily MF attributed to each region and (f) shows the daily MF per unit area.

- We next define additional land regions equatorward of Antarctica, specifically (a) the Southern Andes, including the Falkland Islands, (b) South Georgia, (c) Kerguelen, including Heard Island, (d) Australia including Tasmania, and (e) New Zealand.

- Finally, we divide the remaining area into a Drake Passage region (55°-80°W) and a general ocean region covering all remaining areas within 6,000 km of the pole.

All defined land regions include a 200 km coastline padding on interfaces with the ocean, as discussed above. Figure 11b shows the proportion of area that each region makes up. The general ocean region covers the vast majority of this region, making up 78% of the area; second largest is the East Antarctic region at 7%, then the Antarctic Peninsula at 5%. At the other end of the scale, small islands such as Kerguelen and South Georgia cover ∼0.4% and ∼0.2% of the total area.

In Figure 11c, we show the percentage of absolute MF attributed to each region. This is computed by considering the location each ray is backward traced to and weighting this by the observed absolute MF of this ray at its stratospheric start point. For simplicity we scale by the total observed stratospheric MF over May–September (not time-varying values). MF peaks in mid-winter in July, when almost 35% of the overall observed MF across the May–September period is measured.

We clearly see that waves traced to sources over the ocean make up the largest proportion of MF in the stratosphere. The split between orographic and non-orographic sources vary significantly between months: in May, the split between orographic and non-orographic is even, whereas in July MF from non-orographic regions contributes almost two thirds of the total MF observed.

This mix is also illustrated by Figure 11e, where we show the same absolute MF traced to regions (similar to Figure 11c, but as a daily time series smoothed with a 7-day moving mean). We again see that the MF traced to the ocean dominates and peaks in mid-winter. The second largest-contributing region is the Southern Andes (gray) which shows some temporal variability. In the later winter, that is, from day 80 onward, East Antarctica becomes an important source of MF, overtaking the Southern Andes on occasion.

In Figures 11d and 11f, we scale the MF traced back to each region by the area of the region, normalizing each time series to a maximum of one. This quantifies the MF originating in each region per unit area. We find that waves traced to the ocean contribute only a very small amount of MF per unit area to the total, whereas, consistent with our expectations from previous studies, the Southern Andes (gray) contribute the highest MF per unit area across all months. Small islands such as Kerguelen (brown) and South Georgia (yellow) contribute a disproportionately high percentage of observed MF per unit area compared to other regions. Alexander and Grimsdell (2013) carried out a comprehensive analysis of GW activity observed by AIRS over 14 islands in the Southern Ocean and concluded that including these island waves in climate models could contribute a significant fraction of the missing drag on Southern Hemisphere winds. They found that the MF originating from these islands varied across the winter season, in agreement with our results. Eckermann et al. (2016) studied the dynamics of orographic GWs observed in the mesosphere over the Auckland Islands (50.7°S 166.1°E) using the aircraft-based Advanced Mesospheric Temperature Mapper they concluded that orographic GW drag due to subantarctic islands contributes to the overall momentum budget and controlling the middle atmospheric dynamics.

Figure 11d shows that the Drake Passage region (light blue) contributes a much higher MF per unit area than the rest of the sea (blue). As discussed in Section 4.4, this is likely a combination of high-MF orographic events that have been mis-traced to the Drake Passage instead of the large sources of the Southern Andes and Antarctic Peninsula, non-orographic activity from storms in the Drake Passage region or orographic-jet induced GWs.

In Figure 11f, we show MF per unit area smoothed with a 7-day moving mean. Despite this smoothing, the strong intermittency of different sources can still be seen, in agreement with previous observational studies on intermittency (J. H. Jiang et al., 2002; Minamihara et al., 2020; Wright et al., 2013, 2017; and others). In particular, Kerguelen (brown), South Georgia (yellow) and New Zealand (red) exhibit seemingly periodic activity, which may be related to lower-stratospheric planetary waves modulating GW excitation and also influencing the visibility of these waves to AIRS. Vertical GW propagation from tropospheric sources into the middle atmosphere over New Zealand was studied extensively during the DEEPWAVE campaign (e.g., Bramberger et al., 2017; Fritts et al., 2016; Kaifler et al., 2015; and many others). Kaifler et al. (2015) carried out a detailed study of GW activity over New Zealand using observations from the ground-based TELMA lidar (Temperature Lidar for Middle Atmosphere Research) during winter and spring 2014 (covering the DEEPWAVE campaign period). They found that GW activity over New Zealand was dominated by individual events of 1–3 days duration alternating with quieter periods. Conversely, in our results, MF peaks in roughly 20-day periods, this is possibly due to observational filter effects with different instruments seeing different parts of the GW spectrum.

Table 2
Percentage of Monthly Stratospheric Absolute Momentum Flux (Observed by AIRS at 39 km Altitude), Separated by Region Traced Back To

	May	June	July	August	September	Average
Sea	39%	57%	58%	47%	43%	49%
Drake Passage	9.0%	8.0%	4.9%	5.9%	6.6%	6.9%
Total non-orographic	48%	65%	63%	53%	50%	56%
Southern Andes	31%	20%	10%	10%	17%	18%
East Antarctica	7.7%	5.8%	13%	17%	17%	12%
Transantarctic region	4.7%	0.9%	5.5%	11%	8.7%	6.1%
Antarctic Peninsula	6.7%	3.2%	6.7%	7.8%	6.1%	6.1%
Kerguelen	1.6%	1.4%	0.9%	0.3%	0.1%	0.9%
New Zealand	0.3%	2.0%	0.6%	0.1%	0.0%	0.6%
South Georgia	0.5%	0.4%	0.3%	0.5%	0.7%	0.5%
Australia	0.1%	0.9%	0.4%	0.1%	0.0%	0.3%
Total orographic	53%	35%	37%	47%	50%	44%

Note. Rounded to 2 significant figures.

Finally, we quantify the contribution of MF from the different regions in Table 2. This shows the percentage of total observed monthly MF attributed to each region. On average, 56% of absolute MF traces back to the ocean, while 44% is traced back to land. This means that orographic sources contribute much more MF per unit area and as a result appear as hotspots of activity, whereas non-orographic GW activity contributes more to the overall observed MF. This proportion varies temporally, with orographic sources contributing as much as 53% in May and as little as 35% in June to the total. With the MF estimations it is important to note that, as discussed previously, due to the observational filter of AIRS and its increased sensitivity to longer vertical wavelengths. When waves over the Southern Ocean get refracted to longer vertical wavelengths by the strong winds of the stratospheric polar vortex, this then increases their visibility to AIRS and would increase the estimations of amplitude and hence momentum fluxes. The waves from wave sources further away from the polar vortex (e.g., New Zealand and Australia) do not experience this refraction to longer vertical wavelengths and hence the momentum fluxes attributed to these regions is likely an underestimate due to the limitations of the AIRS instrument.

This is the first time that the relative contributions of these sources to the total observed MF have been quantified. For context, using stratosphere-level data only, Hindley et al. (2019) attributed 20%–37% of the zonal MF observed by AIRS between 68 and 35°S to the Southern Andes throughout June, July, and August by comparing the observed zonal total to the fraction observed in the 80–55°W longitude range. Our work significantly expands upon this by 1 employing ray-tracing methods to push the calculation back from the stratosphere to the source level and by 2 quantifying all plausible source regions contributing to this belt. The Southern Andes, as expected, is the largest land source and contributes 10%–31%; next strongest are the East Antarctic region (5.8%–17%) and the Trans-antarctic region (1%–11%). The large range on each of these values represents the significant seasonal variability at play: the Antarctic Peninsula contributes the same to the total observed MF on average as the Transantarctic region (6.1%) but with a much more consistent range (3.2%–7.8%). Kerguelen's contributes 0.1%–1.6% to the monthly average, with New Zealand just behind at 0.0%–0.7%. This zero lower-bound is because in September there was almost no contribution to the total observed MF, most likely due to the positioning of the jet away from New Zealand in that month, we also note that this is likely an underestimate due to the visibility effects of AIRS measurements discussed previously. Finally, South Georgia and Australia contribute 0.3%–0.7% and 0.1%–0.9% across the winter months.

5. Conclusions

In this work, we have backward ray-traced all AIRS polar winter observations of GWs over Antarctica and the surrounding area for the period May – September 2012. We note that due to the observational filter of AIRS there will be MF in the stratosphere that is either underestimated or not visible to AIRS and this MF is not considered in this work. However, AIRS is sensitive to GWs with longer vertical wavelengths and shorter horizontal wavelengths which carry the majority of MF.

We use these 14.2 million traced waves to systematically explore the meridional propagation and downstream propagation of waves from lower atmospheric sources. We examine the spatial split between orographically and non-orographically generated waves, and, for the first time, explicitly quantify the contributions of different source regions to the overall observed MF. Our key conclusions are:

- Waves converge over the Southern Ocean at all longitudes, and not just over the Andes and Antarctic Peninsula. We measure an average meridional propagation distance ∼500 km from tropospheric sources to ∼40 km of altitude.
- Waves observed thousands of km downstream of the Southern Andes, Antarctic Peninsula, Transantarctic Mountains, Prince Charles Mountains, Kerguelen, South Georgia, and New Zealand can be traced back to distant sources. Such downstream propagation of these orographic waves is highly dependent on the

background stratospheric wind, this could be partly due to the strong winds of the jet refracting the waves to longer vertical wavelengths and increasing their observability to AIRS.

- Of those waves which trace back to sources over the ocean, we see a pattern dominated by strong non-orographic GW activity at all longitudes around 60°S, except for the region between ≈20°W and ≈10°E. In future work with this data set, we will specifically investigate the role of non-orographic sources in the southern high latitudes.
- We analyze the proportion of orographic and non-orographic MF that is observed in the stratosphere at different latitudes. On average, of the MF observed near 60°S, orographic sources are responsible for ∼5%–35%, likely made up of a combination of laterally propagating waves and small island sources. However, the large remaining percentage, suggesting that non-orographic sources are more important in contributing to the MF observed here.
- Finally, we quantify the proportion of observed stratospheric MF that is traced back to different regions within 6,000 km of the pole. The Southern Andes is the largest orographic source, contributing between ∼10%–30% of the total. This is followed by sources on the Antarctic Continent. The small islands of Kerguelen and South Georgia also contribute to the total overall monthly mean MF observed across this whole area, despite only making up <1% of the land area.

Our work provides strong observational evidence of GW behavior across the winter Southern Hemisphere and quantifies the propagation and momentum fluxes from different sources to aid future GW parametrizations.

Data Availability Statement

The 3-D AIRS temperature retrieval used in this work is described in Hoffmann and Alexander (2009) and is publicly available at Hoffmann (2021) [Dataset]. ERA5 reanalysis used is also publicly available (Copernicus Climate Change Service, 2017).

Acknowledgments
This study is supported by the UK Natural Environment Research Council (NERC) under Grant NE/W003201/1(PN, CW, and NH), NE/W003317/1(TMG), and NE/S00985X/1(NH and CW). NH is supported by an NERC Independent Research Fellowship NE/X0178. CW is also supported by NERC grant NE/V01837X/1 as well as a Royal Society University Research Fellowship URF/R/221023, Royal Society grants RGF/EA/180217 and RF/ERE/210079. PN is supported by an NERC GW4+ Doctoral Training Partnership studentship (NE/S007504/1). PB is supported by a University of Bath studentship. The authors gratefully acknowledge the University of Bath's Research Computing Group (https://doi.org/10.15125/b6cd-s854) for their support in this work.

References

Alexander, M. J. (1998). Interpretations of observed climatological patterns in stratospheric gravity wave variance. *Journal of Geophysical Research*, *103*(D8), 8627–8640. https://doi.org/10.1029/97jd03325

Alexander, M. J., & Barnet, C. (2007). Using satellite observations to constrain parameterizations of gravity wave effects for global models. *Journal of the Atmospheric Sciences*, *64*(5), 1652–1665. https://doi.org/10.1175/JAS3897.1

Alexander, M. J., Eckermann, S. D., Broutman, D., & Ma, J. (2009). Momentum flux estimates for South Georgia Island mountain waves in the stratosphere observed via satellite. *Geophysical Research Letters*, *36*(12), L12816. https://doi.org/10.1029/2009GL038587

Alexander, M. J., Geller, M., McLandress, C., Polavarapu, S., Preusse, P., Sassi, F., et al. (2010). Recent developments in gravity-wave effects in climate models and the global distribution of gravity-wave momentum flux from observations and models. *Quart. J. Roy. Meteor. Soc.*, *136*(650, A), 1103–1124. https://doi.org/10.1002/qj.637

Alexander, M. J., Gille, J., Cavanaugh, C., Coffey, M., Craig, C., Eden, T., et al. (2008). Global estimates of gravity wave momentum flux from high resolution dynamics limb sounder observations. *Journal of Geophysical Research*, *113*(D15), 0148–0227. https://doi.org/10.1029/2007jd008807

Alexander, M. J., & Grimsdell, A. W. (2013). Seasonal cycle of orographic gravity wave occurrence above small islands in the Southern Hemisphere: Implications for effects on the general circulation. *Journal of Geophysical Research*, *118*(20), 11589–11599. https://doi.org/10.1002/2013JD020526

Amemiya, A., & Sato, K. (2016). A new gravity wave parameterization including three-dimensional propagation. *Journal of the Meteorological Society of Japan. Ser. II*, *94*(3), 237–256. https://doi.org/10.2151/jmsj.2016-013

Anstey, J. A., & Shepherd, T. G. (2014). High-latitude influence of the quasi-biennial oscillation. *Quarterly Journal of the Royal Meteorological Society*, *140*(678), 1–21. https://doi.org/10.1002/qj.2132

Aumann, H., Chahine, M., Gautier, C., Goldberg, M., Kalnay, E., McMillin, L., et al. (2003). AIRS/amsu/hsb on the aqua mission: Design, science objectives, data products, and processing systems. *IEEE Transactions on Geoscience and Remote Sensing*, *41*(2), 253–264. https://doi.org/10.1109/TGRS.2002.808356

Banyard, T. P., Wright, C. J., Hindley, N. P., Halloran, G., Krisch, I., Kaifler, B., & Hoffmann, L. (2021). Atmospheric gravity waves in Aeolus wind lidar observations. *Geophysical Research Letters*, *48*(10). https://doi.org/10.1029/2021GL092756

Bramberger, M., Dörnbrack, A., Bossert, K., Ehard, B., Fritts, D. C., Kaifler, B., et al. (2017). Does strong tropospheric forcing cause large-amplitude mesospheric gravity waves? A DEEPWAVE case study. *Journal of Geophysical Research*, *122*(21), 11422–11443. https://doi.org/10.1002/2017JD027371

Chahine, M. T., Pagano, T. S., Aumann, H. H., Atlas, R., Barnet, C., Bblaisdell, J., et al. (2006). AIRS: Improving weather forecasting and providing new data on greenhouse gases. *Bulletin of the American Meteorological Society*, *87*(7), 911–926. https://doi.org/10.1175/BAMS-87-7-911

Copernicus Climate Change Service. (2017). *ERA5: Fifth generation of ECMWF atmospheric reanalyses of the global climate*. European Centre For Medium-Range Weather Forecasts (ECMWF). Retrieved from https://cds.climate.copernicus.eu/

de la Cámara, A., Lott, F., Jewtoukoff, V., Plougonven, R., & Hertzog, A. (2016). On the gravity wave forcing during the southern stratospheric final warming in LMDZ. *Journal of the Atmospheric Sciences*, *73*(8), 3213–3226. https://doi.org/10.1175/jas-d-15-0377.1

Dörnbrack, A., Eckermann, S. D., Williams, B. P., & Haggerty, J. (2022). Stratospheric gravity waves excited by a propagating Rossby wave train—A DEEPWAVE case study. *Journal of the Atmospheric Sciences*, *79*(2), 567–591. https://doi.org/10.1175/JAS-D-21-0057.1

Dunkerton, T. J. (1984). Inertia–Gravity waves in the stratosphere. *Journal of the Atmospheric Sciences*, *41*(23), 3396–3404. https://doi.org/10.1175/1520-0469(1984)041⟨3396:IWITS⟩2.0.CO;2

Eckermann, S. D., Broutman, D., Ma, J., Doyle, J. D., Pautet, P.-D., Taylor, M. J., et al. (2016). Dynamics of orographic gravity waves observed in the mesosphere over the Auckland Islands during the deep propagating gravity wave experiment (DEEPWAVE). *Journal of the Atmospheric Sciences*, *73*(10), 3855–3876. https://doi.org/10.1175/JAS-D-16-0059.1

Eckermann, S. D., & Marks, C. J. (1997). Grograt: A new model of the global propagation and dissipation of atmospheric gravity waves. *Advances in Space Research*, *20*(6), 1253–1256. (Coupling and Energetics in the Stratosphere-Mesosphere-Thermosphere- Ionosphere System). https://doi.org/10.1016/S0273-1177(97)00780-1

Eckermann, S. D., & Preusse, P. (1999). Global measurements of stratospheric mountain waves from Space. *Science*, *286*(5444), 1534–1537. https://doi.org/10.1126/science.286.5444.1534

Ehard, B., Kaifler, B., Dörnbrack, A., Preusse, P., Eckermann, S. D., Bramberger, M., et al. (2017). Horizontal propagation of large-amplitude mountain waves into the polar night jet. *Journal of Geophysical Research: Atmospheres*, *122*(3), 1423–1436. https://doi.org/10.1002/2016JD025621

Eichinger, R., Rhode, S., Garny, H., Preusse, P., Pisoft, P., Kuchař, A., et al. (2023). Emulating lateral gravity wave propagation in a global chemistry–climate model (EMAC v2.55.2) through horizontal flux redistribution. *Geoscientific Model Development*, *16*(19), 5561–5583. https://doi.org/10.5194/gmd-16-5561-2023

Ern, M., Preusse, P., Alexander, M. J., & Warner, C. D. (2004). Absolute values of gravity wave momentum flux derived from satellite data. *Journal of Geophysical Research*, *109*(D20), D20103. https://doi.org/10.1029/2004JD004752

Ern, M., Trinh, Q. T., Preusse, P., Gille, J. C., Mlynczak, M. G., III, J. M. R., & Riese, M. (2018). GRACILE: A comprehensive climatology of atmospheric gravity wave parameters based on satellite limb soundings. *Earth System Science Data*, *10*(2), 857–892. https://doi.org/10.5194/essd-10-857-2018

Fritts, D. C., & Alexander, M. J. (2003). Gravity wave dynamics and effects in the middle atmosphere. *Reviews of Geophysics*, *41*(1), 1003. https://doi.org/10.1029/2001RG000106

Fritts, D. C., Riggin, D. M., Balsley, B. B., & Stockwell, R. G. (1998). Recent results with an MF radar at McMurdo, Antarctica: Characteristics and variability of motions near 12-hour period in the mesosphere. *Geophysical Research Letters*, *25*(3), 297–300. https://doi.org/10.1029/97GL03702

Fritts, D. C., Smith, R. B., Taylor, M. J., Doyle, J. D., Eckermann, S. D., Dörnbrack, A., et al. (2016). The deep propagating gravity wave experiment (DEEPWAVE): An airborne and ground-based exploration of gravity wave propagation and effects from their sources throughout the lower and middle atmosphere. *Bulletin of the American Meteorological Society*, *97*(3), 425–453. https://doi.org/10.1175/BAMS-D-14-00269.1

Garcia, R. R., Smith, A. K., Kinnison, D. E., de la Camara, A., & Murphy, D. J. (2017). Modification of the gravity wave parameterization in the whole atmosphere community climate model: Motivation and results. *Journal of the Atmospheric Sciences*, *74*(1), 275–291. https://doi.org/10.1175/JAS-D-16-0104.1

Garfinkel, C. I., & Oman, L. D. (2018). Effect of gravity waves from small islands in the southern ocean on the southern hemisphere atmospheric circulation. *Journal of Geophysical Research: Atmospheres*, *123*(3), 1552–1561. https://doi.org/10.1002/2017JD027576

Geldenhuys, M., Kaifler, B., Preusse, P., Ungermann, J., Alexander, P., Krasauskas, L., et al. (2023). Observations of gravity wave refraction and its causes and consequences. *Journal of Geophysical Research: Atmospheres*, *128*(3), e2022JD036830. https://doi.org/10.1029/2022JD036830

Geldenhuys, M., Preusse, P., Krisch, I., Zülicke, C., Ungermann, J., Ern, M., et al. (2021). Orographically induced spontaneous imbalance within the jet causing a large-scale gravity wave event. *Atmospheric Chemistry and Physics*, *21*(13), 10393–10412. https://doi.org/10.5194/acp-21-10393-2021

Geller, M., Alexander, M. J., Love, P., Bacmeister, J., Ern, M., Hertzog, A., et al. (2013). A comparison between gravity wave momentum fluxes in observations and climate models. *Journal of Climate*, *26*(17), 6383–6405. https://doi.org/10.1175/JCLI-D-12-00545.1

Goldberg, M., Qu, Y., McMillin, L., Wolf, W., Zhou, L., & Divakarla, M. (2003). AIRS near-real-time products and algorithms in support of operational numerical weather prediction. *Geoscience and Remote Sensing, IEEE Transactions on*, *41*, 379–389. https://doi.org/10.1109/TGRS.2002.808307

Green, B., Sheshadri, A., Alexander, M. J., Bramberger, M., & Lott, F. (2024). Gravity wave momentum fluxes estimated from Project Loon balloon data. *Journal of Geophysical Research: Atmospheres*, *129*(5), e2023JD039927. https://doi.org/10.1029/2023JD039927

Gupta, A., Birner, T., Dörnbrack, A., & Polichtchouk, I. (2021). Importance of gravity wave forcing for springtime southern polar vortex breakdown as revealed by ERA5. *Geophysical Research Letters*, *48*(10), e2021GL092762. https://doi.org/10.1029/2021GL092762

Gupta, A., Reichert, R., Dörnbrack, A., Garny, H., Eichinger, R., Polichtchouk, I., et al. (2024). Estimates of southern hemispheric gravity wave momentum fluxes across observations, reanalyses, and kilometer-scale numerical weather prediction model. *Journal of the Atmospheric Sciences*, *81*(3), 583–604. https://doi.org/10.1175/jas-d-23-0095.1

Hasha, A., Bühler, O., & Scinocca, J. (2008). Gravity wave refraction by three-dimensionally varying winds and the global transport of angular momentum. *Journal of the Atmospheric Sciences*, *65*(9), 2892–2906. https://doi.org/10.1175/2007JAS2561.1

Hendricks, E., Doyle, J., Eckermann, S. D., Jiang, Q., & Reinecke, P. (2014). What is the source of the stratospheric gravity wave belt in austral winter? *Journal of the Atmospheric Sciences*, *71*(5), 1583–1592. https://doi.org/10.1175/JAS-D-13-0332.1

Hersbach, H., Bell, B., Berrisford, P., Hirahara, S., Horányi, A., Muñoz-Sabater, J., et al. (2020). The ERA5 global reanalysis. *Quarterly Journal of the Royal Meteorological Society*, *146*(730), 1999–2049. https://doi.org/10.1002/qj.3803

Hertzog, A., Alexander, M. J., & Plougonven, R. (2012). On the intermittency of gravity wave momentum flux in the stratosphere. *Journal of the Atmospheric Sciences*, *69*(11), 3433–3448. https://doi.org/10.1175/JAS-D-12-09.1

Hertzog, A., Boccara, G., Vincent, R. A., Vial, F., & Cocquerez, P. (2008). Estimation of gravity wave momentum flux and phase speeds from quasi-Lagrangian stratospheric balloon flights. Part II: Results from the Vorcore campaign in Antarctica. *Journal of the Atmospheric Sciences*, *65*(10), 3056–3070. https://doi.org/10.1175/2008JAS2710.1

Hindley, N. P., Smith, N. D., Wright, C. J., Rees, D. A. S., & Mitchell, N. J. (2016). A two-dimensional Stockwell transform for gravity wave analysis of AIRS measurements. *Atmospheric Measurement Techniques*, *9*(6), 2545–2565. https://doi.org/10.5194/amt-9-2545-2016

Hindley, N. P., Wright, C. J., Gadian, A. M., Hoffmann, L., Hughes, J. K., Jackson, D. R., et al. (2021). Stratospheric gravity waves over the mountainous island of South Georgia: Testing a high-resolution dynamical model with 3-D satellite observations and radiosondes. *Atmospheric Chemistry and Physics*, *21*(10), 7695–7722. https://doi.org/10.5194/acp-21-7695-2021

Hindley, N. P., Wright, C. J., Hoffmann, L., Moffat-Griffin, T., & Mitchell, N. J. (2020). An 18-year climatology of directional stratospheric gravity wave momentum flux from 3-D satellite observations. *Geophysical Research Letters*, *47*(22), e2020GL089557. https://doi.org/10.1029/2020gl089557

Hindley, N. P., Wright, C. J., Smith, N. D., Hoffmann, L., Holt, L. A., Alexander, M. J., et al. (2019). Gravity waves in the winter stratosphere over the Southern Ocean: High-resolution satellite observations and 3-D spectral analysis. *Atmospheric Chemistry and Physics*, *19*(24), 15377–15414. https://doi.org/10.5194/acp-19-15377-2019

Hindley, N. P., Wright, C. J., Smith, N. D., & Mitchell, N. J. (2015). The southern stratospheric gravity wave hot spot: Individual waves and their momentum fluxes measured by COSMIC GPS-RO. *Atmospheric Chemistry and Physics*, *15*(14), 7797–7818. https://doi.org/10.5194/acp-15-7797-2015

Hoffmann, L. (2021). AIRS/Aqua observations of gravity waves [Dataset]. https://doi.org/10.26165/JUELICH-DATA/LQAAJA

Hoffmann, L., & Alexander, M. J. (2009). Retrieval of stratospheric temperatures from Atmospheric Infrared Sounder radiance measurements for gravity wave studies. *Journal of Geophysical Research*, *114*(D7), D07105. https://doi.org/10.1029/2008JD011241

Hoffmann, L., Alexander, M. J., Clerbaux, C., Grimsdell, A. W., Meyer, C. I., Roessler, T., & Tournier, B. (2014). Intercomparison of stratospheric gravity wave observations with AIRS and IASI. *Atmospheric Measurement Techniques*, *7*(12), 4517–4537. https://doi.org/10.5194/amt-7-4517-2014

Hoffmann, L., Grimsdell, A. W., & Alexander, M. J. (2016). Stratospheric gravity waves at southern Hemisphere orographic hotspots: 2003–2014 AIRS/Aqua observations. *Atmospheric Chemistry and Physics*, *16*(14), 9381–9397. https://doi.org/10.5194/acp-16-9381-2016

Hoffmann, L., Xue, X., & Alexander, M. J. (2013). A global view of stratospheric gravity wave hotspots located with Atmospheric Infrared Sounder observations. *Journal of Geophysical Research*, *118*(2), 416–434. https://doi.org/10.1029/2012JD018658

Holt, L. A., Alexander, M. J., Coy, L., Liu, C., Molod, A., Putman, W., & Pawson, S. (2017). An evaluation of gravity waves and gravity wave sources in the Southern Hemisphere in a 7km global climate simulation. *Quarterly Journal of the Royal Meteorological Society*, *143*(707), 2481–2495. https://doi.org/10.1002/qj.3101

Holt, L. A., Brabec, C. M., & Alexander, M. J. (2023). Exploiting high-density zonal-sampling of HIRDLS profiles near 60°S to investigate missing drag in chemistry-climate models. *Journal of Geophysical Research: Atmospheres*, *128*(8), e2022JD037398. https://doi.org/10.1029/2022JD037398

Jewtoukoff, V., Hertzog, A., Plougonven, R., de la Camara, A., & Lott, F. (2015). Comparison of gravity waves in the southern hemisphere derived from balloon observations and the ECMWF analyses. *Journal of the Atmospheric Sciences*, *72*(9), 3449–3468. https://doi.org/10.1175/JAS-D-14-0324.1

Jiang, J. H., Wu, D. L., & Eckermann, S. D. (2002). Upper Atmosphere Research Satellite (UARS) MLS observation of mountain waves over the Andes. *Journal of Geophysical Research*, *107*(D20). SOL 15-1-SOL 15-10. https://doi.org/10.1029/2002JD002091

Jiang, Q., Doyle, J. D., Eckermann, S. D., & Williams, B. P. (2019). Stratospheric trailing gravity waves from New Zealand. *Journal of the Atmospheric Sciences*, *76*(6), 1565–1586. https://doi.org/10.1175/JAS-D-18-0290.1

Kaifler, B., Kaifler, N., Ehard, B., Dörnbrack, A., Rapp, M., & Fritts, D. C. (2015). Influences of source conditions on mountain wave penetration into the stratosphere and mesosphere. *Geophysical Research Letters*, *42*(21), 9488–9494. https://doi.org/10.1002/2015gl066465

Krasauskas, L., Kaifler, B., Rhode, S., Ungermann, J., Woiwode, W., & Preusse, P. (2023). Oblique propagation and refraction of gravity waves over the Andes observed by GLORIA and ALIMA during the SouthTRAC campaign. *Journal of Geophysical Research: Atmospheres*, *128*(10), e2022JD037798. https://doi.org/10.1029/2022JD037798

Krisch, I., Preusse, P., Ungermann, J., Dörnbrack, A., Eckermann, S. D., Ern, M., et al. (2017). First tomographic observations of gravity waves by the infrared limb imager GLORIA. *Atmospheric Chemistry and Physics*, *17*(24), 14937–14953. https://doi.org/10.5194/acp-17-14937-2017

Llamedo, P., Salvador, J., de la Torre, A., Quiroga, J., Alexander, P., Hierro, R., et al. (2019). 11 years of Rayleigh lidar observations of gravity wave activity above the southern tip of south America. *Journal of Geophysical Research: Atmospheres*, *124*(2), 451–467. https://doi.org/10.1029/2018JD028673

Marks, C. J., & Eckermann, S. D. (1995). A three-dimensional nonhydrostatic ray-tracing model for gravity waves: Formulation and preliminary results for the middle atmosphere. *Journal of the Atmospheric Sciences*, *52*(11), 1959–1984. https://doi.org/10.1175/1520-0469(1995)052⟨1959:ATDNRT⟩2.0.CO;2

McDonald, A. J. (2012). Gravity wave occurrence statistics derived from paired COSMIC/FORMOSAT3 observations. *Journal of Geophysical Research*, *117*(D15), D15106. https://doi.org/10.1029/2011JD016715

McLandress, C., Shepherd, T. G., Polavarapu, S., & Beagley, S. R. (2012). Is missing orographic gravity wave drag near 60°S the cause of the stratospheric zonal wind biases in chemistry–climate models? *Journal of the Atmospheric Sciences*, *69*(3), 802–818. https://doi.org/10.1175/JAS-D-11-0159.1

McLandress, C., Shepherd, T. G., Scinocca, J. F., Plummer, D. A., Sigmond, M., Jonsson, A. I., & Reader, M. C. (2011). Separating the dynamical effects of climate Change and ozone depletion. Part II: Southern Hemisphere troposphere. *Journal of Climate*, *24*(6), 1850–1868. https://doi.org/10.1175/2010JCLI3958.1

Minamihara, Y., Sato, K., & Tsutsumi, M. (2020). Intermittency of gravity waves in the Antarctic troposphere and lower stratosphere revealed by the PANSY radar observation. *Journal of Geophysical Research: Atmospheres*, *125*(15), e2020JD032543. https://doi.org/10.1029/2020JD032543

Moffat-Griffin, T., Colwell, S. R., Wright, C. J., Hindley, N. P., & Mitchell, N. J. (2020). Radiosonde observations of a wintertime meridional convergence of gravity waves around 60°S in the lower stratosphere. *Geophysical Research Letters*, *47*(20), e2020GL089740. https://doi.org/10.1029/2020GL089740

Perrett, J., Wright, C. J., Hindley, N. P., Hoffmann, L., Mitchell, N. J., Preusse, P., & et al (2020). Determining gravity wave sources and propagation in the southern hemisphere by ray-tracing AIRS measurements. *Geophysical Research Letters*, *48*(2). https://doi.org/10.1029/2020GL088621

Plougonven, R., de la Cámara, A., Hertzog, A., & Lott, F. (2020). How does knowledge of atmospheric gravity waves guide their parameterizations? *Quarterly Journal of the Royal Meteorological Society*, *146*(728), 1529–1543. https://doi.org/10.1002/qj.3732

Plougonven, R., Hertzog, A., & Guez, L. (2013). Gravity waves over Antarctica and the Southern Ocean: Consistent momentum fluxes in mesoscale simulations and stratospheric balloon observations. *Quart. J. Roy. Meteor. Soc.*, *139*(670), 101–118. https://doi.org/10.1002/qj.1965

Plougonven, R., Jewtoukoff, V., de la Cámara, A., Lott, F., & Hertzog, A. (2017). On the relation between gravity waves and wind speed in the lower stratosphere over the southern ocean. *Journal of the Atmospheric Sciences*, *74*(4), 1075–1093. https://doi.org/10.1175/JAS-D-16-0096.1

Polichtchouk, I., Shepherd, T. G., Hogan, R. J., & Bechtold, P. (2018). Sensitivity of the brewer-dobson circulation and polar vortex variability to parameterized nonorographic gravity wave drag in a high-resolution atmospheric model. *Journal of the Atmospheric Sciences*, *75*(5), 1525–1543. https://doi.org/10.1175/jas-d-17-0304.1

Pramitha, M., Kumar, K. K., Ratnam, M. V., Praveen, M., & Rao, S. V. B. (2020). Gravity wave source spectra appropriation for mesosphere lower thermosphere using meteor radar observations and GROGRAT model simulations. *Geophysical Research Letters*, *47*(19), e2020GL089390. https://doi.org/10.1029/2020GL089390

Preusse, P., Dörnbrack, A., Eckermann, S., Riese, M., Schaeler, B., Bacmeister, J. T., et al. (2002). Space-based measurements of stratospheric mountain waves by CRISTA 1. Sensitivity, analysis method, and a case study. *Journal of Geophysical Research*, *107*(D23), 8178. https://doi.org/10.1029/2001JD000699

Preusse, P., Eckermann, S. D., Ern, M., Oberheide, J., Picard, R. H., Roble, R. G., et al. (2009). Global ray tracing simulations of the saber gravity wave climatology. *Journal of Geophysical Research*, *114*(D8). https://doi.org/10.1029/2008JD011214

Preusse, P., Ern, M., Bechtold, P., Eckermann, S. D., Kalisch, S., Trinh, Q. T., & Riese, M. (2014). Characteristics of gravity waves resolved by ECMWF. *Atmospheric Chemistry and Physics*, *14*(19), 10483–10508. https://doi.org/10.5194/acp-14-10483-2014

Pulido, M., Rodas, C., Dechat, D., & Lucini, M. M. (2013). High gravity-wave activity observed in Patagonia, Southern America: Generation by a cyclone passage over the Andes mountain range. *Quarterly Journal of the Royal Meteorological Society*, *139*(671), 451–466. https://doi.org/10.1002/qj.1983

Rapp, M., Kaifler, B., Dörnbrack, A., Gisinger, S., Mixa, T., Reichert, R., et al. (2021). SOUTHTRAC-GW: An airborne field campaign to explore gravity wave dynamics at the world's strongest hotspot. *Bulletin of the American Meteorological Society*, *102*(4), E871–E893. https://doi.org/10.1175/BAMS-D-20-0034.1

Rhode, S., Preusse, P., Ern, M., Ungermann, J., Krasauskas, L., Bacmeister, J., & Riese, M. (2023). A mountain ridge model for quantifying oblique mountain wave propagation and distribution. *Atmospheric Chemistry and Physics*, *23*(14), 7901–7934. https://doi.org/10.5194/acp-23-7901-2023

Sato, K., Tateno, S., Watanabe, S., & Kawatani, Y. (2011). Gravity wave characteristics in the southern hemisphere revealed by a high-resolution middle-atmosphere general circulation model. *Journal of the Atmospheric Sciences*, *69*(4), 1378–1396. https://doi.org/10.1175/JAS-D-11-0101.1

Strube, C., Preusse, P., Ern, M., & Riese, M. (2021). Propagation paths and source distributions of resolved gravity waves in ECMWF-IFS analysis fields around the southern polar night jet. *Atmospheric Chemistry and Physics Discussions*, *2021*(24), 1–39. https://doi.org/10.5194/acp-2021-160

Suneeth, K. V., & Das, S. S. (2020). Zonally resolved water vapour coupling with tropical tropopause temperature: Seasonal and interannual variability, and influence of the walker circulation. *Climate Dynamics*, *54*(11–12), 4657–4673. https://doi.org/10.1007/s00382-020-05255-w

Voelker, G. S., Bölöni, G., Kim, Y.-H., Zängl, G., & Achatz, U. (2024). Ms-gwam: A 3-dimensional transient gravity wave parametrization for atmospheric models. *Journal of the Atmospheric Sciences*, *81*(7), 1181–1200. https://doi.org/10.1175/JAS-D-23-0153.1

Vosper, S. B. (2015). Mountain waves and wakes generated by South Georgia: Implications for drag parametrization. *QJRMS*, *141*(692), 2813–2827. https://doi.org/10.1002/qj.2566

Watanabe, S., Kawatani, Y., Tomikawa, Y., Miyazaki, K., Takahashi, M., & Sato, K. (2008). General aspects of a T213L256 middle atmosphere general circulation model. *Journal of Geophysical Research*, *113*(D12), D12110. https://doi.org/10.1029/2008JD010026

Wei, J., Zhang, F., Richter, J. H., Alexander, M. J., & Sun, Y. Q. (2022). Global distributions of tropospheric and stratospheric gravity wave momentum fluxes resolved by the 9-km ECMWF experiments. *Journal of the Atmospheric Sciences*, *79*(10), 2621–2644. https://doi.org/10.1175/JAS-D-21-0173.1

Wrasse, C. M., Nakamura, T., Takahashi, H., Medeiros, A. F., Taylor, M. J., Gobbi, D., et al. (2006). Mesospheric gravity waves observed near equatorial and low-middle latitude stations: Wave characteristics and reverse ray tracing results. *Annales Geophysicae*, *24*(12), 3229–3240. https://doi.org/10.5194/angeo-24-3229-2006

Wright, C. J., & Gille, J. C. (2013). Detecting overlapping gravity waves using the S-Transform. *Geophysical Research Letters*, *40*(9), 1850–1855. https://doi.org/10.1002/grl.50378

Wright, C. J., Hindley, N. P., Alexander, M. J., Holt, L. A., & Hoffmann, L. (2021). Using vertical phase differences to better resolve 3D gravity wave structure. *Atmospheric Measurement Techniques*, *14*(9), 5873–5886. https://doi.org/10.5194/amt-14-5873-2021

Wright, C. J., Hindley, N. P., Hoffmann, L., Alexander, M. J., & Mitchell, N. J. (2017). Exploring gravity wave characteristics in 3-D using a novel S-transform technique: AIRS/Aqua measurements over the Southern Andes and Drake Passage. *Atmospheric Chemistry and Physics*, *17*(13), 8553–8575. https://doi.org/10.5194/acp-17-8553-2017

Wright, C. J., Hindley, N. P., Moss, A. C., & Mitchell, N. J. (2016). Multi-instrument gravity-wave measurements over Tierra del Fuego and the Drake Passage - Part 1: Potential energies and vertical wavelengths from AIRS, COSMIC, HIRDLS, MLS-Aura, SAAMER, SABER and radiosondes. *Atmospheric Measurement Techniques*, *9*(3), 877–908. https://doi.org/10.5194/amt-9-877-2016

Wright, C. J., Osprey, S. M., & Gille, J. C. (2013). Global observations of gravity wave intermittency and its impact on the observed momentum flux morphology. *Journal of Geophysical Research*, *118*(19), 10980–10993. https://doi.org/10.1002/jgrd.50869

Wu, D. L. (2004). Mesoscale gravity wave variances from AMSU-A radiances. *Geophysical Research Letters*, *31*(12), 1944–8007. https://doi.org/10.1029/2004GL019562

Wu, D. L., & Eckermann, S. D. (2008). Global gravity wave variances from Aura MLS: Characteristics and interpretation. *Journal of the Atmospheric Sciences*, *65*(12), 3695–3718. https://doi.org/10.1175/2008JAS2489.1